MNRAS **443,** 2285–2310 (2014) doi:10.1093/mnras/stu1296

Optimal integrated abundances for chemical tagging of extragalactic globular clusters★

Charli M. Sakari,[1]†‡ Kim Venn,[1] Matthew Shetrone,[2] Aaron Dotter[3] and Dougal Mackey[3]

[1]*Department of Physics and Astronomy, University of Victoria, Victoria, BC V8W 3P2, Canada*
[2]*McDonald Observatory, University of Texas at Austin, HC75 Box 1337-MCD, Fort Davis, TX 79734, USA*
[3]*Research School of Astronomy and Astrophysics, The Australian National University, Weston, ACT 2611, Australia*

Accepted 2014 June 26. Received 2014 June 25; in original form 2014 May 6

ABSTRACT

High-resolution integrated light (IL) spectroscopy provides detailed abundances of distant globular clusters whose stars cannot be resolved. Abundance comparisons with other systems (e.g. for chemical tagging) require understanding the systematic offsets that can occur between clusters, such as those due to uncertainties in the underlying stellar population. This paper analyses high-resolution IL spectra of the Galactic globular clusters 47 Tuc, M3, M13, NGC 7006, and M15 to (1) quantify potential systematic uncertainties in Fe, Ca, Ti, Ni, Ba, and Eu and (2) identify the most stable abundance ratios that will be useful in future analyses of unresolved targets. When stellar populations are well modelled, uncertainties are ∼0.1–0.2 dex based on sensitivities to the atmospheric parameters alone; in the worst-case scenarios, uncertainties can rise to 0.2–0.4 dex. The [Ca I/Fe I] ratio is identified as the optimal integrated [α/Fe] indicator (with offsets $\lesssim$0.1 dex), while [Ni I/Fe I] is also extremely stable to within $\lesssim$0.1 dex. The [Ba II/Eu II] ratios are also stable when the underlying populations are well modelled and may also be useful for chemical tagging.

Key words: techniques: spectroscopic – globular clusters: individual: M3 – globular clusters: individual: M13 – globular clusters: individual: M15 – globular clusters: individual: NGC 7006 – globular clusters: individual: 47 Tuc.

1 INTRODUCTION

Chemical tagging has been very successful in the Milky Way (MW), enabling the identification of stellar streams and globular clusters (GCs) that were likely accreted from dwarf galaxies and demonstrating that accretion has played some role in the formation of the MW (e.g. Freeman & Bland-Hawthorn 2002; Cohen 2004; Sbordone et al. 2005; Sakari et al. 2011). In order to form a more general picture of galaxy formation, additional systems must be studied; however, similar studies of other massive galaxies are much more difficult to perform because individual stars cannot be resolved for high-resolution spectroscopic observations. These distant systems must therefore be studied through their *integrated light* (IL). GCs are particularly useful for distant IL work, since they appear as bright point sources, and can be observed at greater distances than their individual stars.

The main difficulty in IL studies is interpreting the observations in terms of the physical properties of the underlying stellar population. These difficulties occur largely because of degeneracies in the IL spectra. One way to counter these effects is to calibrate IL analysis techniques to nearby, well-studied systems or theoretical models. For example, IL photometry has been calibrated to GC metallicities (see Brodie & Strader 2006 for a review), while low- to medium-resolution ($R < 5000$) IL spectroscopy has been semi-empirically calibrated for determinations of age, metallicity, and some element abundance ratios (C, N, O, Mg, Na, Ca; e.g. see Schiavon et al. 2002; Lee & Worthey 2005).

Recently, high-resolution ($R > 20\,000$) spectroscopy has been applied to IL studies of Galactic GCs (e.g. McWilliam & Bernstein 2008, hereafter MB08; Colucci et al. 2009; Sakari et al. 2013, hereafter Paper I). These high-resolution studies can be used to improve the precision of the chemical abundance results by examining spectral lines that are less blended and have a range of strengths. Chemical abundances of more elements can be determined as well,

★Based on observations obtained with the Hobby–Eberly Telescope, which is a joint project of the University of Texas at Austin, the Pennsylvania State University, Stanford University, Ludwig-Maximilians-Universität München, and Georg-August-Universität Göttingen.

†E-mail: sakaricm@uvic.ca
‡Vanier Canada Graduate Scholar.

e.g. from neutron capture elements such as Ba and Eu. The program ILABUNDS (presented in MB08) has been tested on Galactic GCs (MB08; Cameron 2009; Paper I) and has been applied to GCs in M31, the Large Magellanic Cloud, Local Group dwarf galaxies, and the early-type galaxy NGC 5128 (Colucci et al. 2009, 2011, 2012, 2013; Colucci & Bernstein 2011). Studies of nearby systems have shown that IL abundances can reproduce the abundances of individual stars and will trace the abundance patterns of field stars that formed in the same environment (for elements that do not vary within clusters). As IL analyses are pushed to more distant systems, they are providing the first detailed studies of chemical enrichment in systems outside the Local Group – for example, IL observations of GCs show that the elliptical galaxy NGC 5128 seems to have undergone rapid chemical enrichment compared to the MW (Colucci et al. 2013).

Abundance results for GCs can be as precise as those from individual stars when determined from high-resolution IL spectra (∼0.1 dex; see Paper 1). However, both kinds of spectroscopic analyses suffer from systematic errors. For individual stars, systematic errors are usually due to the uncertainties in the temperature, gravity, metallicity, and microturbulence of the model atmosphere, and are often added in quadrature (other sources of systematic error exist but are not usually folded into the total error). These systematic errors can occasionally exceed the random abundance errors (McWilliam et al. 1995a), and complicate comparisons of abundance results from various studies. For IL spectra of GCs, a determination of the total systematic errors is more complicated. *Without a general understanding of the systematic errors that occur during an IL analysis, it is extremely difficult to compare IL abundances to those from individual stars, or to those from other GCs, regardless of the precision in the abundances or the quality of the spectra.*

The goal of this paper is to understand and quantify the systematic errors that are present in a typical high-resolution IL spectral analysis. In general, abundance analyses suffer from two different types of systematic uncertainties.

(i) Uncertainties that arise from models, techniques, corrections, or assumptions that apply to all targets in a given study [such as the choice of model atmospheres, the methods for measuring spectral lines, non-local thermodynamic equilibrium (NLTE) corrections, atomic data, etc.]. Such uncertainties can be reduced or eliminated through *differential* analyses.[1]

(ii) Uncertainties that arise from discrepancies between reality and input simplifications or assumptions (e.g. models of the evolved stars or the inclusion of interloping field stars). Such uncertainties will vary between targets, and cannot be removed through differential analyses.

IL spectral analyses suffer from both types of errors. Under the assumptions that each GC's underlying stellar population is known and that model atmospheres can be correctly assigned to the stars in the cluster, most uncertainties should fall under the first type. In reality, however, GC stellar populations cannot be perfectly modelled – moreover, each GC is unique, and the specific deviations from the models will vary from cluster to cluster. Previous authors have investigated the systematic effects on both low- and high-resolution IL spectra as a result of various assumptions about the underlying population. Percival & Salaris (2009) investigated the effects on low-resolution spectral indices as a result of temperature and metallicity scale offsets between the stellar evolution models and the spectral libraries. The effects of improperly modelling particular stellar subpopulations, e.g. the horizontal branch (HB), have also been tested extensively (Schiavon et al. 2004; Colucci et al. 2009; Paper I). This paper goes further, by isolating and investigating the systematic errors that occur when atmospheric parameters are assigned to the stars in the modelled population.

High-resolution IL spectra of the well-studied, resolved Galactic GCs 47 Tuc, M3, M13, NGC 7006, and M15 are used to perform these tests – these GCs span a large range in metallicity and HB morphology and therefore form an ideal test sample. The observations, data reduction, and abundance analysis methods are discussed in Section 2. The original, baseline abundances for comparisons are presented in Section 3. The specific systematic uncertainty tests are described in Appendices A–C; errors that are expected to occur in a colour–magnitude diagram (CMD)-based analysis (for resolved systems) are presented in Appendix A, offsets that may occur in theoretical Hertzsprung–Russell diagram (HRD) analyses (for unresolved systems) are presented in Appendix B, and uncertainties that are expected to occur in both types of analyses (such as potential foreground stars) are described in Appendix C. The results are summarized in Section 4, where the implications of these tests for applications to distant systems are discussed. The best element ratios for IL chemical tagging are also identified.

2 DATA AND ANALYSIS METHODS

2.1 Target selection

The target GCs 47 Tuc, M3, M13, NGC 7006, and M15 were selected to cover a wide range of metallicities (from [Fe/H] ∼ −0.7 to −2.4; Harris 1996) and HB morphologies (from very red to very blue; see Table 1). In particular, M3, M13, and NGC 7006 form a 'second parameter' triad, i.e. the three clusters have approximately the same metallicity, yet have very different HB morphologies. These clusters therefore provide an excellent test set, since the systematic effects of metallicity and HB morphology can be investigated.

2.2 Observations and data reduction

With the exception of 47 Tuc (which was obtained by R. Bernstein and A. McWilliam at the Las Campanas Observatory, or LCO; see MB08), the GC IL spectra were obtained with the High-Resolution Spectrograph (HRS; Tull 1998) on the Hobby–Eberly Telescope (HET; Ramsey et al. 1998; Shetrone et al. 2007) at McDonald Observatory in Fort Davis, TX. The 1-arcsec slit was used, providing an instrumental resolution of $R = 30\,000$. The 600 gr mm^{-1} cross disperser provides wavelength coverage from ∼5320 to 6290 Å on the blue chip and ∼6360 to 7340 Å on the red chip. The large 3-arcsec fibres were scanned across the cluster cores to obtain IL spectra of the central regions (see Table 1 to see how far the coverage extended). More details on the observations can be found in Paper I; the signal-to-noise ratios (S/N) of the final spectra are summarized in Table 1.

As described in Paper I, the data reduction was performed in the Image Reduction and Analysis Facility (IRAF) program.[2]

[1] However, some of these uncertainties may depend on GC properties such as metallicity.

[2] IRAF is distributed by the National Optical Astronomy Observatory, which is operated by the Association of Universities for Research in Astronomy, Inc., under cooperative agreement with the National Science Foundation.

Table 1. Basic information about the target GCs.

Cluster	$[Fe/H]_{lit}$	HB index	S/N[a] (5500 Å)	S/N[a] (7000 Å)	$v_{helio,\,obs}$ (km s^{-1})	$v_{helio,\,lit}$ (km s^{-1})	σ_{obs} (km s^{-1})	σ_{lit} (km s^{-1})	$r^{b}_{IL\ spectra}$ (r_c)
47 Tuc[c]	−0.70	−0.99	120	180	–	–	11.50 ± 0.30[d]	11.0	1.1
M3	−1.60	0.08	180	230	−146.0 ± 1.1	−147.6	5.66 ± 0.15	5.5	1.8
M13	−1.60	0.97	130	250	−247.5 ± 1.3	−244.2	7.23 ± 0.33	7.1	1.7
NGC 7006	−1.50	−0.28	65	130	−380.4 ± 0.7	−384.1	4.49 ± 0.60	–	2.4
M15	−2.40	0.67	95	220	−106.6 ± 0.2	−107.0	12.54 ± 0.60	13.5	7.1

References: more information can be found in Paper I. The [Fe/H] estimates are from isochrone fitting (Dotter et al. 2010; Dotter, Sarajedini & Anderson 2011). The HB index, $(B-R)/(B+V+R)$, comes from Mackey & van den Bergh (2005). Literature values for v_{rad} and σ are from the Harris catalogue (Harris 1996).

[a]S/N (per pixel) are measured in IRAF.

[b]The maximum coverage of the IL spectra, expressed in units of the core radius (which was obtained from Harris 1996).

[c]47 Tuc was observed with the Las Campanas 2.5-m du Pont telescope by R. Bernstein and A. McWilliam; see MB08 for more details.

[d]This velocity dispersion has been determined in the same way as the other GCs, for consistency.

Table 2. The line list.[a]

Wavelength (Å)	Element	EP (eV)	log *gf*	EW (mÅ) Sun	47 Tuc	M3	M13	NGC 7006	M15
5581.979	Ca I	2.523	−0.555	97.0	113.0	50.3	–[b]	63.3	–[b]
5588.764	Ca I	2.526	0.358	–[c]	–[b]	103.7	97.2	124.0	47.0
5590.126	Ca I	2.521	−0.571	–[c]	112.1	58.1	53.9	67.4	–[b]
5601.286	Ca I	2.526	−0.69	–[c]	113.9	56.0	51.7	57.0	–[b]
5857.459	Ca I	2.933	0.24	–[c]	131.0	86.5	74.0	95.0	–[b]

Notes: EWs were measured in DAOSPEC; all strong lines were checked and refined in *splot*. Lines stronger than 150 mÅ were not included in the analysis. Note that this limit may be too high, since some CMD boxes have EWs > 150 mÅ. However, with the exception of 47 Tuc, only a handful of IL spectral lines are stronger than 110 mÅ. Furthermore, none of the clusters shows any noticeable trends in Fe I abundance with EW in the CMD-based analyses.

[a]Table 2 is published in its entirety in the electronic edition of *Monthly Notices of the Royal Astronomical Society*. A portion is shown here for guidance regarding its form and content.

[b]The lines not measured in the target GCs were too weak or were obscured by noises, cosmic rays, etc.

[c]The lines that were not measured in the solar spectrum were those stronger than EW = 150 mÅ; for those lines the solar values of Asplund et al. (2009) were used.

Standard HRS data reduction methods were used, except that bias frame removal was not performed and optimal variance weighting was used during aperture extraction. To subtract the sky, separate sky exposures were taken after each observation; these sky spectra were replaced with continuum fits with the emission lines added back in. Telluric standards were also observed in order to remove telluric absorption lines. The IL spectra were normalized using the continuum fits to an extremely metal-poor (EMP) star, as described in Paper I. The individual spectra were combined using average sigma-clipping routines to mitigate the effects of cosmic rays. Velocity information was determined through cross-correlations with an Arcturus template spectrum (from the Arcturus Atlas;[3] Hinkle 2003), and is also listed in Table 1. More information on the data reduction procedure can be found in Paper I.

2.3 Line list and EW measurements

The spectral lines in this analysis were selected from the IL spectral line lists from MB08 and Colucci et al. (2009) and the red giant branch (RGB) line lists from Sakari et al. (2011) and Venn et al. (2012). Fe, Ca, Ti, Ni, Ba, and Eu lines were selected for this analysis because these elements are useful for chemical tagging purposes. The specific Ca, Ti, Ni, and Ba lines are listed in Table 2, along with the adopted atomic data.

Paper I presented the integrated Fe, Na, Mg, and Eu abundances, and showed that for the target GCs Na, Mg, and Eu are affected by star-to-star variations within the clusters. For that reason, these abundances may not be useful for chemical tagging purposes, and Na and Mg are not considered in this systematic error analysis. Eu is retained, however, as the star-to-star Eu variations within a cluster are not always significant. Roederer (2011) demonstrated that Eu variations are only large for the most massive GCs. Furthermore, these dispersions are not seen in all massive, metal-poor GCs – for instance, Cohen (2011) detect no heavy element dispersion in M92. Ba also varies within some GCs (e.g. M15; Worley et al. 2013); however, again this is likely only the case for the most massive GCs. Furthermore, evidence suggests that Ba and Eu may vary together, such that the ratio of [Ba/Eu] may still be useful for chemical tagging purposes (Worley et al. 2013).

Equivalent widths (EWs) were measured with the automated program DAOSPEC[4] (Stetson & Pancino 2008). Paper I showed that DAOSPEC is capable of reproducing EWs measured in IRAF's *splot* and

[3] ftp://ftp.noao.edu/catalogs/arcturusatlas/

[4] DAOSPEC has been written by P. B. Stetson for the Dominion Astrophysical Observatory of the Herzberg Institute of Astrophysics, National Research Council, Canada.

those measured with the program GETJOB (McWilliam et al. 1995a). Lines stronger than 150 mÅ were removed from the abundance analysis (see the discussions in Paper I; McWilliam et al. 1995b). The Fe EWs are tabulated in Paper I; the EWs for the other lines are shown in Table 2. Eu II has only a single, weak line, and its abundance must be determined via spectrum syntheses (see Paper I). In this case, the EWs that matched the synthesis-based abundances were used for all differential errors analyses in Appendices A–C; these EWs are also listed in Table 2.

2.4 Atmospheric parameters and models

In an IL spectral analysis stellar model atmospheres can either be generated with observed photometry or theoretical isochrones, depending on the target. Nearby clusters have high-quality CMDs, and each star's colour and magnitude can be used to infer its temperature and other atmospheric parameters. This is the method that is used to derive the baseline abundances of the target Galactic GCs (47 Tuc, M3, M13, NGC 7006, and M15), which are presented in Section 3 (see also MB08; Paper I). The stars in very distant clusters, however, cannot be resolved, and isochrones must be used to model the underlying population's HRD.

2.4.1 *Input photometry*

The *Hubble Space Telescope* (*HST*) photometry used in the CMD-based analyses comes from two sources. The 47 Tuc *B*, *V* data is from Guhathakurta et al. (1992) and Howell, Guhathakurta & Gilliland (2000), and was provided by R. Schiavon – this is the same photometry presented in MB08. The *V*, *I* data for all clusters are from the ACS Survey of Galactic Globular Clusters (Sarajedini et al. 2007; Anderson et al. 2008; Dotter et al. 2011). The *HST* magnitudes were converted to Johnson's *V*, *I* magnitudes via the transformations in Sirianni et al. (2005). Stars within the maximum radii observed in the IL spectra were selected for input to ILABUNDS, using the cluster centres from Goldsbury et al. (2010); this circular selection leads to slight discrepancies with the irregular coverage patterns. The CMDs were then binned into boxes, as described in Paper I.

2.4.2 *Input isochrones*

When isolated effects are investigated (e.g. HB morphology; see Appendix B3), the boxes from the input *photometry* are used to simplify the comparisons with the original, CMD-based abundances. For tests that require models of the underlying stellar population, the isochrones from the following sources are considered.

(i) BaSTI/Teramo models (Pietrinferni et al. 2004; Cordier, Pietrinferni & Cassisi 2007) with Ferguson et al. (2005) opacities – the default isochrones utilize extended, $\eta = 0.2$ asymptotic giant branch (AGB) models, though other treatments are investigated.

(ii) Dartmouth Stellar Evolution Database models (DSED; Dotter et al. 2008).

(iii) Victoria–Regina stellar models (VandenBerg, Bergbusch & Dowler 2006).

2.4.3 *Model atmospheres*

Once the atmospheric parameters of a box are known, a corresponding Kurucz model atmosphere[5] (Castelli & Kurucz 2004) is then assigned. The grid values are interpolated to each box's specific $T_{\rm eff}$ and $\log g$.

2.5 Isotopic and hyperfine structure corrections

The isotopic and hyperfine structure (HFS) components for the Ba II lines are from McWilliam (1998) while the Eu II components are from Lawler, Bonvallet & Sneden (2001a) and Lawler et al. (2001b). All HFS corrections were found to be negligible ($\lesssim$0.05 dex) and were not applied to any of the Ba II or Eu II abundances presented in this paper.

2.6 Solar abundances

All of the [Fe/H] and [X/Fe] ratios presented in this paper are calculated *line by line* relative to the solar abundances derived with the EWs in Table 2 and Paper I. These EWs were measured in the solar spectrum ($R = 300\,000$; Kurucz 2005) from the Kurucz (2005) solar flux atlas.[6] Solar atmospheric parameters of $T_{\rm eff} = 5777$ K, $\log g = 4.44$ dex, $\chi = 0.85$ km s^{-1}, and [M/H] = 0.0 were adopted (Yong, Carney & Teixera de Almeida 2005). When the solar lines were stronger than 150 mÅ, Asplund et al. (2009) solar abundances were adopted for those lines.

3 INITIAL ABUNDANCES

The integrated abundances are determined with the EW version of the program ILABUNDS (described in detail in MB08). The initial CMD-based abundances with the standard ILABUNDS input are presented in Table 3. The [Fe/H] and [X/Fe] ratios were calculated differentially *for each line*, using the solar abundances derived from the EWs in Table 2 (see Section 2.6). As in individual stellar analyses, the [X/Fe] ratios are calculated by comparing elements of similar ionization states. Thus, the [X/Fe] ratios of neutral species are relative to Fe I and those of singly ionized species are relative to Fe II.[7] Unless otherwise noted, abundance uncertainties in Appendices A–C are calculated relative to these baseline abundances.

3.1 Random errors

The random abundance errors were calculated as in Shetrone et al. (2003) and Sakari et al. (2011). For each element, three different uncertainties were calculated and compared.

(i) *The line-to-line abundance scatter*. For a single element there is some standard deviation, σ, about the mean abundance. The uncertainty in the mean abundance is therefore $\delta_{\rm X} = \sigma/\sqrt{N}$, where N is the number of spectral lines.

(ii) *The EW uncertainty*. The error of an EW measurement in a particular spectrum can be estimated with the Cayrel (1988) formula; note that an additional 10 per cent EW error is included (see Shetrone et al. 2003; Sakari et al. 2011). The abundances were recalculated with larger and smaller EWs, and the offset in the mean

[5] http://kurucz.harvard.edu/grids.html
[6] http://kurucz.harvard.edu/sun.html
[7] In RGB stars, comparing singly ionized species to Fe II reduces systematic uncertainties, as this compares the dominant ionization stages. IL is dominated by RGB stars, and this methodology is therefore adopted.

Table 3. Initial GC abundances.

	[Fe I/H]	[Fe II/H]	[Ca I/Fe I]	[Ti I/Fe I]	[Ti II/Fe II]	[Ni I/Fe I]	[Ba II/Fe II][a]	[Eu II/Fe II][a, b]
47 Tuc	-0.81 ± 0.02[c]	-0.69 ± 0.07	0.28 ± 0.05	0.27 ± 0.09	0.29 ± 0.07	-0.04 ± 0.07	-0.01 ± 0.08	0.27 ± 0.14
N	68	4	9	6	2	7	2	1
Lit.	−0.72	−0.72	0.19	0.24	0.36	0.0	0.31	0.14 ± 0.03
MB08	-0.75 ± 0.03	-0.72 ± 0.06	0.31 ± 0.08	0.41 ± 0.07	0.54 ± 0.09	0.0 ± 0.06	0.02 ± 0.02	0.04
M3	-1.51 ± 0.02	-1.58 ± 0.05	0.37 ± 0.06	0.30 ± 0.09	0.36 ± 0.06	-0.03 ± 0.08	-0.06 ± 0.09	0.75 ± 0.11
N	95	5	17	6	2	7	3	1
Lit.	−1.50	−1.50	0.27	0.32	0.32	−0.02	0.17	0.51 ± 0.02
M13	-1.57 ± 0.02	-1.55 ± 0.07	0.33 ± 0.06	0.29 ± 0.13	0.42 ± 0.06	-0.02 ± 0.08	0.06 ± 0.08	0.76 ± 0.10
N	71	3	13	6	2	7	3	1
Lit.	−1.53	−1.53	0.26	0.39	0.39	0.02	0.24	0.49 ± 0.03
NGC 7006	-1.52 ± 0.03	-1.56 ± 0.07	0.46 ± 0.12	0.29 ± 0.17	0.33 ± 0.04	-0.04 ± 0.09	0.19 ± 0.08	0.72 ± 0.15
N	73	5	14	7	1	6	3	1
Lit.	−1.52	−1.52	0.30	0.32	0.32	0.02	0.33	0.36 ± 0.02
M15	-2.30 ± 0.03	-2.38 ± 0.10	0.31 ± 0.09	–[d]	0.33 ± 0.12	$+0.01 \pm 0.08$	-0.21 ± 0.06	1.31 ± 0.20
N	31	1	6	–[d]	2	1	3	1
Lit.	−2.37	−2.37	0.27	0.32	0.32	0.01	0.11	0.63 ± 0.03

Notes: [Fe/H] and [X/Fe] values were calculated *line by line* relative to the solar values, as derived with the EWs in Table 2.

References: Literature abundances are from MB08, Pritzl, Venn & Irwin (2005), Sneden et al. (1997), Kraft et al. (1998), Carretta et al. (2004), Jasniewicz et al. (2004), Cohen & Melendez (2005), and the references listed in Paper I.

[a]The Ba and Eu abundances vary between stars in some of these GCs such that the integrated abundances may not match the GC averages.

[b]These abundances were calculated via spectrum syntheses; see Paper I.

[c]47 Tuc's [Fe I/H] abundances are slightly lower than expected, which may be due to the treatment of damping in ILABUNDS (McWilliam, private communication).

[d]M15's Ti I lines were not sufficiently strong to determine a robust [Ti I/Fe I] ratio. To investigate the effects on Ti I at M15's metallicity, EWs were determined to match the [Ti II/Fe II] abundance. These values are only used to calculate M15's systematic offsets in Ti I.

abundance, $\sigma_{\rm EW}$, was divided by $\sqrt{N}$ to give the uncertainty in the mean abundance, $\delta_{\rm EW}$.

(iii) *The iron line-to-line scatter*. Because there are many iron lines, the iron line-to-line scatter provides an estimate of the *minimum* abundance uncertainty, $\delta_{\rm Fe}$. For an element with few detectable spectral lines the above error types may underestimate the true abundance error.

The largest of these three uncertainties ($\delta_{\rm X}$, $\delta_{\rm EW}$, and $\delta_{\rm Fe}$) is adopted as the final *random* abundance error for that element.

3.2 Comparisons with literature abundances

Paper I demonstrated that the EW-based Fe abundances are in excellent agreement with literature values, while the Eu II abundances fall within the literature ranges. Table 3 demonstrates that for the most part the integrated Ca, Ti, Ni, and Ba abundances agree well with the literature abundances from individual stars. The 47 Tuc [Ti I/Fe I] and [Ti II/Fe II] ratios do not agree with the values from MB08 – however, these discrepancies seem to be due to (1) line choice and (2) techniques for calculating differential [X/Fe] ratios.

3.3 Systematic offsets: a description of Appendices A–C

The systematic errors are determined by changing the atmospheric parameters by various amounts, and comparing the new abundances to the original baseline abundances in Table 3 (unless otherwise noted). These differences are calculated as Δ[X/Fe] = [X/Fe] − [X/Fe]$_{\rm orig}$.

The specific details of the systematic errors calculations are presented in Appendices A–C. As discussed in Section 1, the types of systematic uncertainties depend on the analysis type. Appendix A first investigates the errors that only occur in a CMD-based analysis, while Appendix B investigates the uncertainties in an HRD analysis. Appendix C then describes the errors that are present in both types of analyses.

The largest systematic offsets are summarized in Table 4. Offsets $\geq$0.05 dex are in bold. The specific magnitude of the errors can vary between clusters (due to metallicity, HB morphology, etc.). Occasionally the worst-case scenarios are considered, in which case the errors are likely to be upper limits. It is unclear how to combine the individual errors; in particular, it is unclear if all the errors are independent, and should be combined in quadrature.

4 DISCUSSION

IL spectral analyses provide chemical abundances for individual GCs; *high-resolution* IL spectroscopy is particularly well suited for *chemical tagging*. Chemical tagging utilizes detailed chemical abundances to identify chemically peculiar stars and GCs that likely originated in dwarf galaxies (see Freeman & Bland-Hawthorn 2002; Cohen 2004; Sakari et al. 2011). In the MW, detailed abundances and kinematic info can link together individual stars and GCs that were accreted from the same dwarf galaxy. Because of the nature of IL analyses, it may not be possible to link GCs to specific streams – however, it should be possible to separate dwarf-associated GCs from those formed in a massive galaxy. Chemically distinct GCs can only be identified if the abundance ratios are sufficiently robust to systematic uncertainties, ideally within 0.1 dex.[8] This section summarizes the accuracy of each abundance ratio and discusses implications for future extragalactic studies.

[8] For instance, MW halo stars at [Fe/H] $\lesssim -1$ have [α/Fe] = +0.3, while dwarf galaxy stars at similar metallicity have [α/Fe] $\sim$ 0. For a 3σ confirmation that a GC is chemically more like a dwarf galaxy, useful ratios should have systematic errors $\lesssim$0.1 dex.

Table 4. Summary of results.

	Δ[Fe I/H]	Δ[Fe II/H]	Δ[Ca I/Fe I]	Δ[Ti I/Fe I]	Δ[Ti II/Fe II]	Δ[Ni I/Fe I]	Δ[Ba II/Fe II]	Δ[Eu II/Fe II]	Δ[Ba II/Eu II]
CMD-based analyses									
Minimum errors[a]	**≤0.12**	**≤0.20**	**≤0.06**	**≤0.09**	**≤0.14**	≤0.04	**≤0.22**	**≤0.11**	**≤0.17**
CTRs[a, b]	**≤0.07**	≤0.01	≤0.02	≤0.03	≤0.03	≤0.04	**≤0.06**	≤0.04	≤0.04
Input photometry	≤0.04	**≤0.07**	≤0.02	≤0.04	≤0.04	≤0.01	**≤0.07**	≤0.02	**≤0.06**
Incompleteness	**≤0.07**	**≤0.07**	**≤0.05**	**≤0.06**	**≤0.07**	**≤0.04**	**≤0.07**	≤0.03	≤0.04
Sampling[c, d]	**≤0.22**	**≤0.10**	**≤0.09**	–	**≤0.10**	≤0.03	**≤0.21**	**≤0.09**	**≤0.14**
HRD-based analyses									
HRD versus CMD[a]	**≤0.11**	**≤0.19**	**≤0.05**	**≤0.20**	**≤0.10**	≤0.04	**≤0.12**	**≤0.08**	**≤0.10**
Age/[Fe/H] errors[a]	**≤0.16**	**≤0.16**	**≤0.07**	**≤0.12**	**≤0.10**	≤0.04	**≤0.19**	**≤0.08**	**≤0.10**
Diff. isochrones	≤0.02	≤0.04	≤0.02	≤0.02	≤0.01	0.0	≤0.03	≤0.01	≤0.02
IMF	≤0.04	≤0.01	≤0.02	**≤0.06**	**≤0.05**	≤0.02	**≤0.07**	**≤0.05**	≤0.02
Cluster M_V^e	**≤0.36**	**≤0.10**	**≤0.10**	**≤0.41**	**≤0.14**	**≤0.10**	**≤0.33**	**≤0.23**	**≤0.10**
HB morphology[a, d]	**≤0.13**	**≤0.28**	≤0.04	**≤0.17**	**≤0.08**	**≤0.07**	**≤0.14**	**≤0.11**	**≤0.12**
AGB prescription	**≤0.19**	**≤0.15**	**≤0.05**	**≤0.23**	**≤0.09**	**≤0.13**	**≤0.19**	**≤0.14**	**≤0.07**
Blue stragglers	**≤0.07**	**≤0.07**	≤0.02	≤0.04	≤0.04	≤0.03	**≤0.05**	**≤0.06**	≤0.02
Low mass cut-off[a]	**≤0.13**	**≤0.12**	≤0.04	**≤0.24**	**≤0.07**	**≤0.05**	**≤0.11**	**≤0.12**	**≤0.05**
All analyses									
CMD/HRD boxes	≤0.02	≤0.01	≤0.02	≤0.03	≤0.04	≤0.03	≤0.01	**≤0.07**	≤0.04
Microturbulence	**≤0.11**	**≤0.05**	≤0.03	≤0.02	**≤0.08**	**≤0.10**	**≤0.16**	≤0.04	**≤0.16**
LPVs	≤0.01	**≤0.07**	0.0	≤0.03	≤0.01	≤0.03	0.0	0.0	0.0
CH stars[a, d]	0.0	0.0	≤0.01	0.0	0.0	≤0.01	0.0	≤0.01	≤0.01
Hot stars	**≤0.06**	≤0.04	≤0.01	≤0.01	**≤0.07**	≤0.03	≤0.04	≤0.04	**≤0.08**
Field stars[d]	**≤0.10**	**≤0.09**	**≤0.09**	≤0.04	**≤0.07**	**≤0.06**	**≤0.10**	**≤0.05**	**≤0.09**
ODFNEW atms	**≤0.05**	**≤0.12**	≤0.03	≤0.02	≤0.03	≤0.02	≤0.03	≤0.03	≤0.03
CN-cycled atms	**≤0.05**	**≤0.12**	≤0.03	≤0.02	≤0.03	≤0.02	≤0.03	≤0.03	≤0.03

Notes: The errors shown are upper limits from all tests on all clusters. The uncertainties for an individual GC will depend on the properties of the GC.
[a]Metallicity/cluster-dependent result.
[b]The *V*, *I* errors with the Alonso, Arribas & Martínez-Roger (1996, 1999) relations are not considered here; see the text.
[c]These error estimates are specific to M15's wedge-shaped pointing pattern, and are likely to be much higher than would be expected for any extragalactic targets.
[d]Recall that these error estimates consider the worst-case scenario.
[e]These large uncertainties arise in faint GCs due to stochastic sampling of the brightest stars and should be mitigated by considering fractional numbers of stars.

4.1 Summary of results: abundance accuracy

Table 4 provides a summary of the largest effects on the chemical abundance ratios, based on the tests described in Appendices A–C. The values in the table are upper limits; the values only apply to specific cases or worst-case scenarios that will not apply to all GCs. Furthermore, many of the uncertainties vary between clusters as a result of e.g. metallicity or HB effects. From the upper limits in Table 4 it is clear that abundance ratios are more stable to uncertainties than others. The accuracies of the individual abundance ratios are discussed in detail below. Of course, the results presented here are dependent upon the observed lines and their properties, and may vary if different wavelength regions and/or spectral lines are observed.

4.1.1 [Fe/H]

In CMD-based analyses, the largest systematic uncertainties in [Fe I/H] and [Fe II/H] are ∼0.1 and ∼0.2 dex, respectively,[9] for all GCs. The potential HRD-based offsets are much larger, up to ∼0.1–0.4 dex (depending on the GC) for [Fe I/H] and ∼0.2–0.3 dex for [Fe II/H]. The HRD-based offsets are lowest for 47 Tuc, suggesting that red HB, metal-rich GCs may have smaller systematic offsets in HRD-based [Fe/H] ratios.

The [Fe I/H] ratio is particularly sensitive to

(i) sampling of input photometry;
(ii) the usage of isochrones instead of resolved photometry;
(iii) uncertainties in isochrone parameters;
(iv) models of the AGB;
(v) microturbulence variations in the brightest stars;
(vi) the inclusion of bright field stars.

With well-sampled IL spectra and photometry that extends at least to the HB, the uncertainties in the parameters of the brightest stars are reduced, and the individual systematic offsets should be ∼0.1 dex.

The [Fe II/H] ratio is strongly affected by bright RGB stars, AGB and HB stars, hot stars, and model atmosphere chemistries. The offsets tend to be larger for [Fe II/H] than [Fe I/H], and even with partially resolved photometry, the systematic errors in [Fe II/H] remain ∼0.2 dex. This further confirms the suggestion by Colucci et al. (2009) that forcing the [Fe I/H] and [Fe II/H] solutions to be equal will not lead to more accurate isochrone solutions.

[9] The clear offset in the *V*, *I* Alonso et al. (1996, 1999) colour–temperature relations has been neglected.

4.1.2 [Ca/Fe] and [Ti/Fe]

The *largest* [Ca I/Fe I] offsets are ∼0.1 dex, and are due to

(i) sampling of the brightest stars;
(ii) uncertainties in isochrone parameters;
(iii) treatment of the AGB;
(iv) the inclusion of bright field stars.

These results indicate that [Ca I/Fe I] is most affected by the numbers and properties of the bright RGB stars. For the wavelength regions examined here the [Ca I/Fe I] ratio is largely insensitive to the properties of hot stars. With partially resolved GCs and well-sampled IL spectra, the systematic errors in [Ca I/Fe I] should be reduced to $\lesssim$0.1 dex, depending on GC metallicity.

The [Ti I/Fe I] and [Ti II/Fe II] ratios, on the other hand, are very sensitive to uncertainties in the underlying stellar population, with offsets of as much as ∼0.2 dex. Like calcium, [Ti I/Fe I] is sensitive to the numbers and properties of the brightest RGB stars. Ti I is particularly affected in HRD-based analyses: in the initial comparisons with CMD-based abundances, [Ti I/Fe I] is persistently lower than individual stellar values by ∼0.1–0.2 dex (see Appendix B1). When uncertainties in HB morphology and AGB prescription are considered, [Ti I/Fe I] could therefore be uncertain by as much as 0.2–0.4 dex when isochrones are used. In most tests, the [Ti II/Fe II] uncertainties are typically constrained only to within 0.15 dex.

4.1.3 [Ni/Fe]

Since Ni is an iron-peak element with an atomic structure similar to Fe, it is not surprising that the [Ni I/Fe I] is relatively stable to uncertainties in atmospheric parameters – for all tests and GCs, the *highest* systematic uncertainties in [Ni I/Fe I] are only ∼0.1 dex. Nickel appears to be sensitive to both high- and low-mass stars, given that it is most affected by

(i) sampling when the total cluster magnitude is adjusted;
(ii) AGB prescription;
(iii) the HRD low-mass cut-off;
(iv) the presence of field stars.

Despite these sensitivities, however, in general [Ni I/Fe I] is quite robust in both CMD- and HRD-based analyses. With a well-modelled stellar population, the systematic errors in [Ni I/Fe I] approach ∼0.05 dex.

4.1.4 [Ba/Fe] and [Eu/Fe]

Both [Ba II/Fe II] and [Eu II/Fe II] are particularly sensitive to uncertainties in the underlying population, often in similar ways. In CMD-based analyses, [Ba II/Fe II] and [Eu II/Fe II] can be constrained to ∼0.2 and ∼0.1 dex, respectively, for all GCs. The offsets are higher in HRD-based analyses (up to ∼0.3 and ∼0.2, respectively).

Both Ba II and Eu II are sensitive to uncertainties in the brightest RGB stars and red/intermediate HB stars. The strongest effects are caused by

(i) temperature and microturbulence uncertainties, including various microturbulence relations;
(ii) sampling of the brightest stars, whether from uncertain input photometry or from rounding errors in faint clusters;
(iii) isochrone age;
(iv) AGB prescription.

In all clusters, the Ba II and Eu II abundances are insensitive to completeness of the lower main sequence, isochrone offsets, atmospheric [α/Fe], and properties of the blue HB stars.

When Ba and Eu are affected in similar ways, the uncertainties in [Ba/Eu] can be smaller than the individual uncertainties in Ba and Eu. This is true for e.g. uncertainties in the AGB prescription, the total cluster magnitude, and the lower mass cut-off. Thus, in an HRD analysis [Ba/Eu] may have lower systematic errors than the individual [Ba II/Fe II] and [Eu II/Fe II] ratios.

4.2 High resolution versus lower resolution analyses

High-resolution ($R \gtrsim 20\,000$) IL spectral analyses provide two major advantages over lower resolution studies.

(i) More lines can be detected and resolved in a high-resolution spectrum. With more independent measurements, the random errors in individual elemental abundances can be reduced.
(ii) Weaker features can be detected in high-resolution IL spectra, enabling abundances to be obtained for more elements.

Despite these advantages, it requires more observing time to obtain high-resolution IL spectra of a sufficient S/N. This paper has shown that despite the increased precision offered by high-resolution IL spectroscopy, the low accuracy in integrated abundances may render such sharp resolution unnecessary, depending on the science goals.

The cluster metallicity, [Fe/H], is an excellent example for when high resolution may be unnecessary. Although high-resolution IL spectroscopy can reduce random errors in [Fe I/H] to ∼0.02 dex (depending on the S/N), the systematic errors can be as large as ∼0.1–0.4 dex depending on the analysis type, cluster metallicity, etc. Thus, for studies that focus only on [Fe/H] (such as studies of population averages, bimodalities, or gradients; e.g. Caldwell et al. 2011) the increased precision of high resolution offers no benefit. Similarly, for studies of large samples of GCs where the abundances are averaged together, high resolution provides no clear advantage (e.g. average values in certain galaxy types or abundance correlations with GC properties; e.g. Puzia & Sharina 2008; Schiavon et al. 2013).

The strength of high-resolution IL spectroscopy is its ability to provide accurate abundances for individual clusters. High resolution is therefore essential for examining the detailed chemical abundances of GCs, e.g. for chemical tagging studies.

4.3 Optimal abundance ratios for chemical tagging

Based on the offsets presented in Table 4 and the discussion in Section 4.1, certain element ratios are more useful for chemical tagging purposes.

[Fe/H]. Most chemical comparisons require knowledge of the GC metallicity, [Fe/H]. Though the [Fe I/H] ratio can occasionally have large systematic errors, [Fe II/H] consistently also has large offsets, as well as larger statistical errors (because there are fewer Fe II lines). Therefore, in most cases, [Fe I/H] will be the preferable choice to represent the cluster metallicity.

[Ca/Fe]. The [α/Fe] ratio is particularly useful for chemical tagging of dwarf galaxy stars and GCs (see e.g. Venn et al. 2004; Pritzl et al. 2005), where Ca and Ti have both been used as α-indicators in individual stellar analyses. (Though note that the behaviour of Ca and Ti can be very different from other α-elements like O and Mg.) Given that [Ca I/Fe I] is very stable to uncertainties in the underlying stellar population for all GCs considered here, [Ca I/Fe I]

is preferable to [Ti I/Fe I] or [Ti II/Fe II] for probing the [α/Fe] ratios of extragalactic systems.

[Ni/Fe]. The [Ni/Fe] ratio may be useful for identifying chemically peculiar GCs. In particular, Pal 12 and Ter 7, the two metal-rich GCs that were accreted from the Sagittarius dwarf galaxy, are underabundant in [Ni/Fe] like the Sgr field stars (Cohen 2004; Sbordone et al. 2005, 2007). The integrated [Ni I/Fe I] ratios are generally quite stable to abundance uncertainties, and may therefore prove useful for integrated chemical tagging.

[Ba/Fe], [Eu/Fe], [Ba/Eu]. Ba and Eu both form through neutron captures on to iron-peak atoms. In the Sun, 97 per cent of Eu forms from rapid neutron captures (the r-process, i.e. where the neutron flux is so high that the nucleus does not have time to decay between captures) while 85 per cent of Ba forms from slow neutron captures (the s-process; Burris et al. 2000). The nucleosynthetic sites for the two elements (and Fe) therefore differ, and the [Ba/Fe], [Eu/Fe], and [Ba/Eu] ratios differ between stars in the MW and those in dwarf galaxies (see e.g. Venn et al. 2012). Though the systematic uncertainties in [Ba II/Fe II], [Eu II/Fe II], and [Ba II/Eu II] are quite large for all GCs, taken together the three ratios could still prove useful for chemical tagging since all three ratios are unlikely to have simultaneously large offsets.

4.4 CMD- versus HRD-based analyses

Appendix B1 indicates that systematic offsets may occur between CMD- and HRD-based analyses, since the best-fitting HRD-based abundances are not always in agreement with those from a CMD-based analysis (see Table B1), with differences up to 0.2 dex. These differences can be larger than the uncertainties from identifying the best isochrone (i.e. the offsets in Table B1 are sometimes larger than the uncertainties in Table B2). These offsets are likely due to discrepancies between the input isochrone and the true stellar populations – for example, changing the HB morphology can bring [Ti I/Fe I] back into agreement with the CMD-based ratio. However, the necessary alterations to the input isochrones may not be identifiable for unresolved GCs, particularly if the IL spectra are noisy.[10]

Table 4 indicates that if sampling problems are reduced or eliminated then CMD-based chemical abundances are more accurate than HRD-based abundances. This result is driven by the uncertainties in modelling the most evolved stars, notably the tip of the RGB, HB, and AGB stars. However, this approach is not currently feasible for extragalactic targets, for which IL methods are necessary.

Appendix B7 demonstrates that some of the HRD-based offsets disappear when CMDs of the brightest stars are combined with isochrones. This is important for IL analyses of nearby extragalactic GC systems, e.g. GCs in M31 (Mackey et al. 2007, 2013), particularly if those GCs have blue or intermediate HBs. Thus, if accurate and uncontaminated CMDs can be obtained for the brightest stars in a GC, the systematic errors in integrated abundances can be reduced.

4.5 A case study: partially resolved clusters in M31

To illustrate how the results of this paper can be applied to IL studies, Table 5 summarizes the systematic errors for the target clusters *if spectra of this quality were obtained from GCs in M31* and if those GCs had partially resolved *HST* photometry to constrain the age, [Fe/H], HB morphology, AGB prescription, total observed magnitude, and the presence of severely different interloping field stars. The ideal science case would be to perform a chemical tagging analysis on these clusters. Table 5 therefore only shows the systematic uncertainties in the optimal abundance ratios for chemical tagging: [Fe I/H], [Ca I/Fe I], [Ni I/Fe I], [Ba II/Fe II], [Eu II/Fe II], and [Ba II/Eu II]. It is not clear how to combine these errors in a meaningful way – however, if the errors are assumed to be independent then they can be conservatively added together in quadrature (though this may overestimate the errors). These total systematic errors are also shown in Table 5.

As an additional illustration of these errors, the cluster [Ca/Fe] and [Ba/Eu] abundances from Table 3 are compared to MW and dwarf galaxy abundances in Fig. 1, *using the partially resolved systematic errors from Table 5*. The error bars show the total random *and* systematic errors, combined in quadrature. Note that though 47 Tuc has a high [Ba/Eu], it is still consistent with the MW field stars. M15's low [Ba/Eu] ratio is likely due to the star-to-star chemical variations within the massive cluster (see Paper I). With the systematic errors included these Galactic targets would appear consistent with the Galactic field stars, even if they were located at M31's distance. Similarly, GCs associated with dwarf galaxies could be distinguished, even with systematic errors considered, if they are α deficient and/or [Ba/Eu] enhanced.

5 CONCLUSIONS

This paper presents a detailed investigation of the systematic uncertainties in high-resolution integrated abundance analyses that occur when GC stellar populations are modelled. High-resolution HET and LCO IL spectra (covering ~5320–7340 Å) of the Galactic GCs 47 Tuc, M3, M13, NGC 7006, and M15 were combined with *HST* photometry and theoretical isochrones to investigate abundance accuracies over a wide range in metallicity and HB morphology. The stability of Fe, Ca, Ti, Ni, Ba, and Eu abundances is determined through IL analyses with various alterations to the underlying stellar population.

The tests in this paper show the following.

(i) The accuracy in integrated abundances can approach that of individual stellar analyses *if the stellar population is well modelled.* The minimum systematic errors in the abundance ratios are $\lesssim$0.05 dex in [Ca I/Fe I] and [Ni I/Fe I]; $\lesssim$0.1 dex in [Fe II/H], [Ti I/Fe I], [Ti II/Fe II], and [Eu II/Fe II]; and $\lesssim$0.2 dex in [Fe I/H] and [Ba II/Fe II].

(ii) CMD-based analyses are most sensitive to inaccuracies in the input photometry, especially sampling of the brightest stars and incompleteness in the low-mass stars. In the worst-case scenario, the accuracy in integrated CMD-based abundances is $\lesssim$0.1 dex in [Fe II/H], [Ca I/Fe I], [Ti I/Fe I], [Ti II/Fe II], [Ni I/Fe I], and [Eu II/Fe II], and $\lesssim$0.2 dex in [Fe I/H] and [Ba II/Fe II]. It is therefore crucial to select input photometry that matches the regions scanned by IL spectra.

(iii) HRD-based analyses are highly sensitive to sampling of the highest and lowest mass stars, AGB prescription, and HB morphology. The uncertainties can be as high as $\lesssim$0.1 dex in [Ca I/Fe I], [Ti II/Fe II], and [Ni I/Fe I]; $\lesssim$0.2 dex in [Eu II/Fe II]; $\lesssim$0.3 dex in [Fe II/H] and [Ba II/Fe II]; and $\lesssim$0.4 dex in [Fe I/H] and [Ti I/Fe I].

These results have several important implications for IL analyses of extragalactic GCs in distant systems, for both analysis methods.

[10] Noisy IL spectra will lead to a larger dispersion in line-to-line Fe I abundances. A larger dispersion will then complicate the process of minimizing trends with wavelength, reduced EW (REW), and excitation potential (EP).

Table 5. Summary of errors for partially resolved clusters at the distance of M31.

	Δ[Fe I/H]	Δ[Ca I/Fe I]	Δ[Ni I/Fe I]	Δ[Ba II/Fe II]	Δ[Eu II/Fe II]	Δ[Ba II/Eu II]
47 Tuc						
Partially resolved errors	0.09	0.06	0.03	0.04	0.08	0.04
Different isochrones	0.03	0.01	0.01	0.03	0.02	0.02
IMF	0.04	0.02	0.02	0.07	0.05	0.02
Blue stragglers	0.02	0.0	0.01	0.01	0.01	0.0
Low-mass cut-off	0.05	0.04	0.05	0.09	0.12	0.03
Microturbulence relations	0.07	0.01	0.0	0.0	0.04	0.04
LPVs	0.01	0.0	0.03	0.0	0.0	0.0
Field stars	0.09	0.09	0.06	0.10	0.05	0.05
α-enhanced atmospheres	0.05	0.03	0.01	0.01	0.02	0.01
Total[a]	0.17	0.12	0.09	0.16	0.17	0.09
M3						
Partially resolved errors	0.04	0.04	0.06	0.03	0.01	0.02
Different isochrones	0.05	0.02	0.03	0.06	0.03	0.03
IMF	0.02	0.0	0.01	0.02	0.02	0.0
Blue stragglers	0.02	0.0	0.01	0.03	0.06	0.03
Low-mass cut-off	0.10	0.02	0.04	0.11	0.10	0.01
Microturbulence relations	0.04	0.01	0.0	0.01	0.0	0.01
Field stars	0.04	0.0	0.01	0.03	0.04	0.01
α-enhanced atmospheres	0.0	0.01	0.02	0.02	0.01	0.01
Total[a]	0.13	0.05	0.08	0.14	0.13	0.05
M13						
Partially resolved errors	0.05	0.06	0.05	0.07	0.02	0.05
Different isochrones	0.05	0.02	0.03	0.06	0.03	0.03
IMF	0.02	0.0	0.01	0.02	0.02	0.0
Blue stragglers	0.03	0.02	0.02	0.03	0.03	0.0
Low-mass cut-off	0.10	0.01	0.01	0.07	0.08	0.01
Microturbulence relations	0.04	0.01	0.0	0.01	0.0	0.01
Hot stars	0.06	0.01	0.03	0.04	0.04	0.08
Field stars	0.04	0.0	0.01	0.03	0.04	0.01
α-enhanced atmospheres	0.0	0.01	0.02	0.02	0.01	0.01
Total[a]	0.15	0.07	0.07	0.13	0.11	0.06
NGC 7006						
Partially resolved errors	0.04	0.03	0.08	0.04	0.07	0.11
Different isochrones	0.05	0.02	0.03	0.06	0.03	0.03
IMF	0.02	0.0	0.01	0.02	0.02	0.0
Blue stragglers	0.02	0.01	0.01	0.02	0.0	0.02
Low-mass cut-off	0.09	0.0	0.05	0.08	0.09	0.01
Microturbulence relations	0.04	0.01	0.0	0.01	0.0	0.01
Field stars	0.04	0.0	0.01	0.03	0.04	0.01
α-enhanced atmospheres	0.0	0.0	0.01	0.03	0.03	0.0
Total[a]	0.13	0.04	0.10	0.12	0.13	0.12
M15						
Partially resolved errors	0.0	0.01	0.03	0.02	0.01	0.03
Different isochrones	0.05	0.02	0.02	0.05	0.04	0.02
IMF	0.03	0.01	0.02	0.02	0.02	0.02
Blue stragglers	0.07	0.02	0.03	0.05	0.01	0.04
Low-mass cut-off	0.13	0.04	0.01	0.11	0.05	0.06
Microturbulence relations	0.05	0.01	0.03	0.02	0.03	0.0
Hot stars	0.06	0.01	0.03	0.04	0.04	0.08
Field stars	0.10	0.04	0.03	0.07	0.04	0.03
α-enhanced atmospheres	0.02	0.0	0.01	0.0	0.03	0.03
Total[a]	0.20	0.07	0.07	0.16	0.10	0.12

Note: [a]Total errors are conservatively estimated by adding the other errors in quadrature.

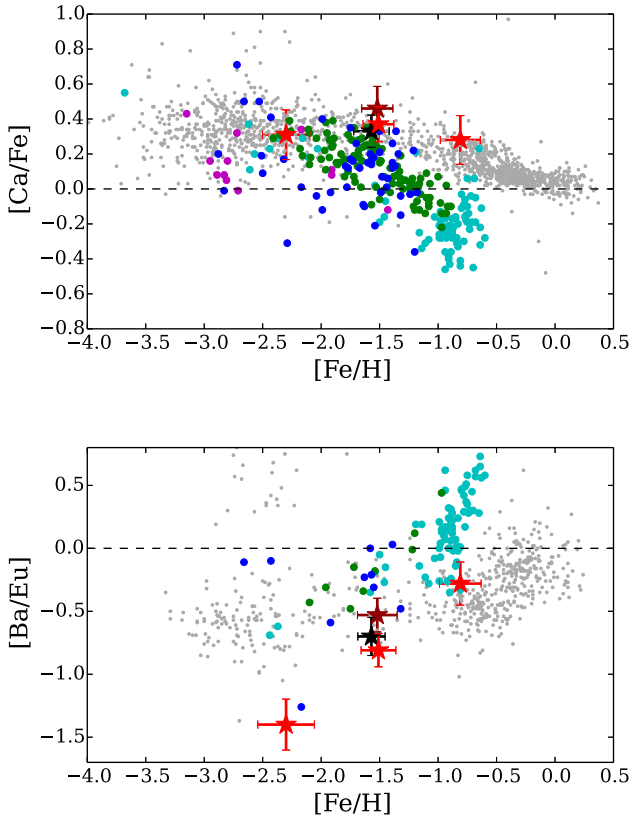

Figure 1. Chemical comparisons between Galactic and dwarf galaxy stars, illustrating that chemical tagging is still possible even when systematic errors are taken into account. The integrated abundances from the target GCs are shown with red stars for 47 Tuc, M3, and M15, with a black star for M13, and with a maroon star for NGC 7006. The error bars are the systematic *and* random errors (added in quadrature), *assuming the GCs were partially resolved at the distance of M31* (see Table 5). The grey points are MW stars. The cyan, green, blue, and magenta points are Fornax, Sculptor, Carina, and Sextans stars, respectively. All points are from the compilation assembled by Venn et al. (2012). This comparison shows that, even including the systematic errors, individual GCs can be chemically tagged based on their integrated abundances, provided that their abundances are distinct from the MW stars.

(i) Certain abundance ratios are less sensitive to systematic uncertainties and are therefore more useful for chemical tagging studies.

(a) The [Fe I/H] ratio should serve as the best [Fe/H] indicator.
(b) The [Ca I/Fe I] ratio is an excellent [α/Fe] indicator.
(c) The [Ni I/Fe I] ratios are very stable to uncertainties.
(d) Individually, [Ba II/Fe II], [Eu II/Fe II], and [Ba II/Eu II] have large systematic uncertainties. Together, however, the three ratios may prove useful for chemical tagging.

(ii) HRD-based abundances may be systematically offset from CMD-based abundances, making comparisons between studies/clusters difficult.

(iii) CMDs of only the brightest stars in a GC can be used to constrain properties of evolved stars, providing more accurate chemical abundance ratios in GCs with blue or intermediate HBs.

(iv) In an HRD-based analysis, high resolution does not provide an advantage for certain abundance ratios, such as [Fe/H]. Lower resolution ($R \lesssim 6500$) IL spectroscopy appears to be sufficient for [Fe/H] determinations, investigations of [Fe/H] distributions, and studies with large sample sizes.

ACKNOWLEDGEMENTS

The authors thank R. Bernstein and A. McWilliam for the use of their 47 Tuc spectrum and their interest in this work. The authors also thank the anonymous referee for suggestions that improved this manuscript. CMS acknowledges funding from the Natural Sciences and Engineering Research Council (NSERC), Canada, via the Vanier CGS program. KV acknowledges funding through the NSERC Discovery Grants program. AD is supported by the Australian Research Council (grant FL110100012). The Hobby–Eberly Telescope is a joint project of the University of Texas at Austin, the Pennsylvania State University, Stanford University, Ludwig-Maximilians-Universität München, and Georg-August-Universität Göttingen. The HET is named in honour of its principal benefactors, William P. Hobby and Robert E. Eberly. The authors wish to thank the night operations staff of the HET for their assistance and expertise with these unusual observations. This work has made use of BaSTI web tools.

REFERENCES

Alonso A., Arribas S., Martínez-Roger C., 1996, A&AS, 117, 227
Alonso A., Arribas S., Martínez-Roger C., 1999, A&AS, 140, 261
Anderson J. et al., 2008, AJ, 135, 2055
Asplund M., Grevesse N., Sauval J. A., Scott P., 2009, ARA&A, 47, 481
Behr B. B., 2003, ApJS, 149, 67
Behr B. B., Cohen J. G., McCarthy J. K., 2000, ApJ, 531, L37
Bond H. E., Neff J. S., 1969, ApJ, 158, 1235
Brodie J. P., Strader J., 2006, ARA&A, 44, 193
Burris D. L., Pilachowski C. A., Armandroff T. E., Sneden C., Cowan J. J., Roe H., 2000, ApJ, 544, 302
Caldwell N., Schiavon R., Morrison H., Rose J. A., Harding P., 2011, AJ, 141, 18
Cameron S., 2009, PhD thesis, Univ. Michigan, Michigan
Carretta E., Gratton R. G., Bragaglia A., Bonifacio P., Pasquini L., 2004, A&A, 416, 925
Carretta E., Bragaglia A., Gratton R., Lucatello S., 2009, A&A, 505, 139
Casagrande L., Ramírez I., Meléndez J., Bessell M., Asplund M., 2010, A&A, 512, 54
Castelli F., Kurucz R. L., 2004, in Piskunov N., Weiss W. W., Gray D. F., eds, Proc. IAU Symp. 210, Modelling of Stellar Atmospheres. Astron. Soc. Pac., San Francisco, p. A20
Cayrel R., 1988, in Cayrel de Strobel G., Spite M., eds, Proc. IAU Symp. 132, The Impact of Very High S/N Spectroscopy on Stellar Physics. Kluwer, Dordrecht, p. 345
Chabrier G., 2003, PASP, 115, 763
Chou M.-Y., Majewski S. T., Cunha K., Smith V. V., Patterson R. J., Martínez-Delgado D., 2010, ApJ, 720, L5
Cohen J., 2004, AJ, 127, 1545
Cohen J. G., 2011, ApJ, 740, L38
Cohen J. G., Melendez J., 2005, AJ, 129, 303
Colucci J. E., Bernstein R. A., 2011, EAS Publ. Ser., 48, 275
Colucci J. E., Bernstein R. A., Cameron S., McWilliam A., Cohen J. G., 2009, ApJ, 704, 385
Colucci J. E., Bernstein R. A., Cameron S. A., McWilliam A., 2011, ApJ, 735, 55
Colucci J. E., Bernstein R. A., Cameron S. A., McWilliam A., 2012, ApJ, 746, 29
Colucci J. E., Duran M. F., Bernstein R. A., McWilliam A., 2013, ApJ, 773, L36
Cordier D., Pietrinferni A., Cassisi S., Salaris M., 2007, AJ, 133, 468
Dotter A., 2008, ApJ, 687, L21
Dotter A., Chaboyer B., Jevremović D., Kostov V., Baron E., Ferguson J. W., 2008, ApJS, 178, 89
Dotter A. et al., 2010, ApJ, 708, 698
Dotter A., Sarajedini A., Anderson J., 2011, ApJ, 738, 74

Ferguson J. W., Alexander D. R., Allard F., Barman T., Bodnarik J. G., Hauschildt P. H., Heffner-Wong A., Tamanai A., 2005, ApJ, 623, 585
Freeman K., Bland-Hawthorn J., 2002, ARA&A, 40, 487
Goldsbury R., Richer H. B., Anderson J., Dotter A., Sarajedini A., Woodley K., 2010, AJ, 140, 1830
Gratton R. G., Carretta E., Castelli F., 1996, A&A, 314, 191
Guhathakurta P., Yanny B., Schneider D. P., Bahcall J. N., 1992, AJ, 104, 1790
Gustafsson B., Edvardsson B., Eriksson K., Jørgensen U. G., Nordlund A., Plez B., 2008, A&A, 486, 951
Harris W. E., 1996, AJ, 112, 1487 (2010 edition)
Helmi A., White S. D. M., 1999, MNRAS, 307, 495
Hinkle K., Wallace L., Livingston W., Ayres T., Harmer D., Valenti J., 2003, in Brown A., Harper G. M., Ayres T. R., eds, The Future of Cool-Star Astrophysics: 12th Cambridge Workshop on Cool Stars, Stellar Systems, and the Sun. University of Colorado, p. 851
Howell J. H., Guhathakurta P., Gilliland R. L., 2000, PASP, 112, 1200
Jasniewicz G., de Laverny P., Parthasarathy M., Lèbre A., Thévenin F., 2004, A&A, 423, 353
Kirby E. N., Guhathakurta P., Bolte M., Sneden C., Geha M. C., 2009, ApJ, 705, 328
Kraft R. P., Sneden C., Smith G. H., Shetrone M. D., Fulbright J., 1998, AJ, 115, 1500
Kroupa P., 2002, Science, 295, 82
Kurucz R. L., 2005, Mem. Soc. Astron. Ital., 8, 189
Lawler J. E., Bonvallet G., Sneden C., 2001a, ApJ, 556, 452
Lawler J. E., Wickliffe M. E., den Hartog E. A., Sneden C., 2001b, ApJ, 563, 1075
Lee H.-C., Worthey G., 2005, ApJS, 160, 176
Lee H.-C., Yoon S.-J., Lee Y.-W., 2000, AJ, 120, 998
Lovisi L., Mucciarelli A., Lanzoni B., Ferraro F. R., Gratton R., Dalessandro E., Contreras Ramos R., 2012, ApJ, 754, 91
Mackey A. D., van den Bergh S., 2005, MNRAS, 360, 631
Mackey A. D. et al., 2007, ApJ, 655, L85
Mackey A. D. et al., 2013, ApJ, 770, 17
McWilliam A., 1998, AJ, 115, 1640
McWilliam A., Bernstein R., 2008, ApJ, 684, 326 (MB08)
McWilliam A., Preston G. W., Sneden C., Shectman S., 1995a, AJ, 109, 2736
McWilliam A., Preston G. W., Sneden C., Searle L., 1995b, AJ, 109, 2757
Maraston C., 2005, MNRAS, 362, 799
Ocvirk P., 2010, ApJ, 709, 88
Percival S. M., Salaris M., 2009, ApJ, 703, 1123
Percival S., Salaris M., 2011, MNRAS, 412, 2445
Pietrinferni A., Cassisi S., Salaris M., Castelli F., 2004, ApJ, 612, 168
Pritzl B. J., Venn K. A., Irwin M., 2005, AJ, 130, 2140
Puzia T. H., Sharina M. E., 2008, ApJ, 674, 909
Ramirez I., Melendez J., 2005, ApJ, 626, 465
Ramsey L. W. et al., 1998, Proc. SPIE, 3352, 34
Robin A. C., Reylé C., Derrière S., Picaud S., 2003, A&A, 409, 523
Roederer I. U., 2011, ApJ, 732, L17
Sakari C. M., Venn K. A., Irwin M., Aoki W., Arimoto N., Dotter A., 2011, ApJ, 740, 106
Sakari C. M., Shetrone M., Venn K., McWilliam A., Dotter A., 2013, MNRAS, 434, 358 (Paper I)
Salpeter E. E., 1955, ApJ, 121, 161
Sarajedini A. et al., 2007, AJ, 133, 1658
Sbordone L., Bonifacio P., Marconi G., Buonanno R., Zaggia S., 2005, A&A, 437, 905
Sbordone L., Bonifacio P., Buonanno R., Marconi G., Monaco L., Zaggia S., 2007, A&A, 465, 815
Schiavon R. P., Faber S. M., Castilho B. V., Rose J. A., 2002, ApJ, 580, 850
Schiavon R. P., Rose J. A., Courteau S., MacArthur L. A., 2004, ApJ, 608, L33
Schiavon R. P., Caldwell N., Conroy C., Graves G. J., Strader J., MacArthur L. A., Courteau S., Harding P., 2013, ApJ, 776, L7
Shetrone M. D., Smith G. H., Briley M. M., Sandquist E., Kraft R. P., 1999, PASP, 111, 1115
Shetrone M., Venn K., Tolstory E., Primas F., Hill V., Kaufer A., 2003, AJ, 125, 684
Shetrone M. D. et al., 2007, PASP, 119, 556
Sirianni M. et al., 2005, PASP, 117, 1049
Sneden C., Kraft R. P., Shetrone M. D., Smith G. H., Langer G. E., Prosser C. F., 1997, AJ, 114, 1964
Sneden C., Kraft R. P., Guhathakurta P., Peterson R. C., Fulbright J., 2004, AJ, 127, 2162
Stetson P. B., Pancino E., 2008, PASP, 120, 1332
Tull R. G., 1998, Proc. SPIE, 3355, 387
VandenBerg D. A., Bergbusch P. A., Dowler P. D., 2006, ApJS, 162, 375
VandenBerg D. A., Brogaard K., Leaman R., Casagrande L., 2013, ApJ, 775, 134
Venn K. A., Irwin M., Shetrone M. D., Tout C. A., Hill V., Tolstoy E., 2004, AJ, 128, 1177
Venn K. A. et al., 2012, ApJ, 751, 102
Worley C. C., Hill V., Sobeck J., Carretta E., 2013, A&A, 553, A47
Yong D., Carney B. W., Teixera de Almeida M. L., 2005, AJ, 130, 597

APPENDIX A: SYSTEMATIC OFFSETS THAT OCCUR IN A CMD-BASED ANALYSIS

The stars in nearby clusters can be fully resolved (like the Galactic GCs studied here) or partially resolved (such as the GCs surrounding M31; see Mackey et al. 2007). If the colours and magnitudes of the brightest stars are known, they can be directly converted to temperatures and surface gravities, avoiding the problems associated with attempting to model the underlying stellar population.

The main advantage of a CMD-based analysis is that the basic properties (i.e. age and [Fe/H]) may be estimated from the CMD. The distribution of stars in the CMD is also known, removing the need to model difficult subpopulations (e.g. the HB or the AGB) or the relative numbers of dwarfs and giants. The main disadvantages of a CMD-based analysis are that observable properties must be converted to intrinsic, physical quantities and that the CMDs do not completely represent the observed regions. Errors in observed quantities can lead to cluster-to-cluster systematic errors, while differences in the employed conversion techniques/relations can lead to systematic offsets between studies. Discrepancies between photometric and spectroscopic observations (e.g. sampled regions or incompleteness) can also lead to systematic uncertainties, as can poor resolution in cluster cores.

This appendix investigates the systematic errors in integrated abundances that occur only when using a CMD. Two sources of error are considered.

(i) Errors that occur when observable quantities are converted to physical values (Appendices A1–A3).

(ii) Errors that occur when the input photometry does not exactly match the population observed in the IL spectra (Appendices A3–A5; also see Appendix C).

A1 Minimum errors in photometric parameters

Conversions to photometric stellar parameters require estimates of a cluster's distance modulus, reddening, turn-off mass, etc., all of which have associated uncertainties that lead to unavoidable minimum uncertainties in the photometric effective temperature, $T_{\rm eff}$, and surface gravity, $\log g$. Detailed abundance analyses with individual stars also show that the spectroscopically determined microturbulence, ξ, and metallicity, [Fe/H], cannot be perfectly constrained. These errors in the atmospheric parameters are typically on the order of $\Delta T_{\rm eff} = \pm 100$ K, $\Delta \log g = \pm 0.2$ dex, $\Delta \xi = \pm 0.2$ km s^{-1}, and $\Delta[M/H] = \pm 0.1$ dex *regardless of the methods used to determine these parameters* (see e.g. Sakari et al. 2011). These abundance

Table A1. The offsets in the CMD-based abundances due to uncertainties in the atmospheric parameters.

		Δ[Fe I/H]	Δ[Fe II/H]	Δ[Ca I/Fe I]	Δ[Ti I/Fe I]	Δ[Ti II/Fe II]	Δ[Ni I/Fe I]	Δ[Ba II/Fe II]	Δ[Eu II/Fe II]
47 Tuc	$+\Delta T$	+0.04	**−0.10**	+0.04	**+0.07**	**+0.07**	0.0	**+0.10**	**+0.07**
	$-\Delta T$	−0.03	**+0.11**	−0.04	**−0.08**	**−0.07**	0.0	**−0.11**	−0.06
	$+\Delta\log g$	+0.01	**+0.10**	−0.02	0.0	−0.02	+0.03	−0.03	−0.02
	$-\Delta\log g$	−0.02	**−0.11**	+0.03	+0.02	+0.03	−0.02	+0.04	+0.03
	$+\Delta\xi$	**−0.09**	**−0.05**	−0.01	+0.02	**−0.07**	+0.01	**−0.11**	+0.02
	$-\Delta\xi$	**+0.08**	**+0.06**	+0.03	0.0	**+0.07**	+0.01	**+0.11**	−0.04
	$+\Delta$[M/H]	0.0	+0.03	0.0	0.0	−0.01	+0.01	0.0	0.0
	$-\Delta$[M/H]	−0.02	−0.04	+0.03	+0.02	+0.01	0.0	+0.01	0.0
M3	$+\Delta T$	**+0.08**	**−0.05**	0.0	**+0.06**	+0.04	0.0	**+0.07**	**+0.05**
	$-\Delta T$	**−0.06**	**+0.07**	−0.02	**−0.09**	−0.04	0.0	**−0.07**	−0.03
	$+\Delta\log g$	−0.01	**+0.09**	−0.02	0.0	−0.02	+0.02	−0.04	+0.01
	$-\Delta\log g$	+0.01	**−0.08**	+0.01	−0.01	+0.02	−0.03	+0.03	+0.02
	$+\Delta\xi$	**−0.05**	−0.02	−0.02	+0.01	**−0.05**	0.0	**−0.12**	+0.02
	$-\Delta\xi$	**+0.05**	+0.03	+0.01	−0.02	**+0.05**	+0.01	**+0.11**	+0.01
	$+\Delta$[M/H]	0.0	+0.04	−0.01	−0.02	−0.01	+0.01	−0.01	+0.02
	$-\Delta$[M/H]	0.0	−0.01	0.0	0.0	+0.01	0.0	−0.01	0.0
M13	$+\Delta T$	**+0.09**	**−0.05**	−0.01	**+0.05**	+0.03	−0.01	**+0.07**	**+0.05**
	$-\Delta T$	**−0.07**	**+0.07**	0.0	**−0.07**	−0.04	0.0	**−0.08**	−0.02
	$+\Delta\log g$	0.0	**+0.09**	−0.02	−0.01	−0.02	+0.02	−0.04	+0.02
	$-\Delta\log g$	+0.01	**−0.08**	+0.02	0.0	+0.02	−0.02	+0.03	+0.02
	$+\Delta\xi$	**−0.05**	−0.03	−0.01	+0.02	−0.04	0.0	**−0.10**	+0.03
	$-\Delta\xi$	**+0.06**	+0.03	0.0	−0.03	**+0.05**	−0.01	**+0.10**	+0.02
	$+\Delta$[M/H]	0.0	+0.03	0.0	−0.01	−0.01	0.0	0.0	+0.03
	$-\Delta$[M/H]	0.0	−0.02	+0.01	+0.01	+0.01	0.0	0.0	+0.02
NGC 7006	$+\Delta T$	**+0.08**	**−0.06**	+0.01	**+0.05**	+0.04	0.0	**+0.09**	**+0.05**
	$-\Delta T$	**−0.07**	**+0.06**	−0.02	**−0.07**	−0.04	0.0	**−0.07**	−0.03
	$+\Delta\log g$	−0.01	**+0.08**	−0.02	0.0	−0.01	+0.03	−0.03	+0.01
	$-\Delta\log g$	+0.01	**−0.08**	+0.02	0.0	+0.01	−0.02	+0.04	+0.01
	$+\Delta\xi$	**−0.06**	−0.03	+0.02	+0.03	−0.03	+0.01	**−0.11**	+0.02
	$-\Delta\xi$	**+0.06**	+0.02	+0.01	−0.03	**+0.05**	0.0	**+0.12**	+0.01
	$+\Delta$[M/H]	0.0	+0.03	−0.01	−0.02	0.0	+0.01	+0.01	+0.01
	$-\Delta$[M/H]	0.0	−0.02	0.0	0.0	+0.01	0.0	0.0	0.0
M15	$+\Delta T$	**+0.10**	−0.03	−0.04	+0.02	+0.03	+0.02	**+0.06**	**+0.07**
	$-\Delta T$	**−0.11**	+0.02	+0.03	−0.02	−0.02	−0.02	**−0.06**	−0.02
	$+\Delta\log g$	−0.03	**+0.06**	0.0	+0.01	−0.01	+0.02	−0.02	+0.02
	$-\Delta\log g$	+0.02	**−0.07**	0.0	0.0	+0.01	−0.01	+0.01	+0.02
	$+\Delta\xi$	**−0.06**	−0.01	+0.01	**+0.06**	−0.02	+0.03	**−0.09**	+0.01
	$-\Delta\xi$	**+0.06**	0.0	−0.01	**−0.05**	+0.04	−0.03	**+0.11**	+0.03
	$+\Delta$[M/H]	−0.01	0.0	0.0	0.0	+0.01	0.0	+0.01	+0.03
	$-\Delta$[M/H]	+0.01	−0.01	−0.01	0.0	0.0	0.0	0.0	+0.01
47 Tuc	ΔT, $\log g$	–	**<0.20**	**<0.06**	–	–	<0.04	–	–
	ΔT, ξ	**<0.12**	–	–	**<0.06**	**<0.14**	–	**<0.22**	**<0.11**

Notes: The uncertainties in the atmospheric parameters are the typical values found in individual stellar analyses: $\Delta T = \pm 100$ K, $\Delta\log g = \pm 0.2$ dex, $\Delta\xi = \pm 0.2$ km s^{-1}, and Δ[M/H] = ±0.1 dex. The last two rows tabulate the maximum abundance differences that occur when two parameters are changed together. Abundance differences are calculated relative to the baseline abundances in Table 3, as described in Section 3.3. Significant offsets (≥0.05 dex) are in bold.

differences are therefore good estimates of the minimum systematic errors that would occur in a CMD-based IL abundance analysis.

These minimum changes to the atmospheric parameters lead to the abundances shown in Table A1. Significant errors (≥0.05 dex) are in bold. Note that the surface gravity and microturbulence were changed independently from each other, even though the microturbulence is determined through an empirical relationship with the surface gravity.[11] With the empirical relation, a change in the surface gravity of $\Delta\log g = 0.2$ dex would only lead to a $\Delta\xi = 0.04$ km s^{-1}.

[11] The effects of the microturbulence relation are investigated in Appendix C2.

The abundance differences in Table A1 indicate that

(i) the largest differences in [Fe/H] and [X/Fe] are ∼0.1 dex;

(ii) the model atmosphere metallicity has a negligible effect on all abundance ratios;

(iii) the differences in the [Fe I/H] and [Fe II/H] ratios are generally <0.1 dex, except in 47 Tuc and M15, where offsets are ∼0.1 dex;

(iv) the [Fe I/H] and [Fe II/H] ratios can be significantly (i.e. $|\Delta$[Fe/H]$| > 0.05$) affected by the changes in temperature, surface gravity, and microturbulence;

(v) the relative [Ca I/Fe I] and [Ni I/Fe I] ratios are largely unaffected by these errors in the atmospheric parameters;

Table A2. Differences in CMD-based abundance ratios with various CTRs.

	Δ[Fe I/H]	Δ[Fe II/H]	Δ[Ca I/Fe I]	Δ[Ti I/Fe I]	Δ[Ti II/Fe II]	Δ[Ni I/Fe I]	Δ[Ba II/Fe II]	Δ[Eu II/Fe II]
47 Tuc								
Extrapolated A96/99	0.0	0.0	0.0	0.0	0.0	0.0	0.0	+0.01
RM05	−0.01	+0.01	−0.01	−0.03	−0.01	0.0	−0.02	0.0
C10+RM05	+0.01	0.0	+0.01	0.0	+0.01	0.0	+0.01	+0.01
Kurucz only	**+0.08**	−0.04	+0.03	**+0.05**	**+0.07**	+0.01	**+0.10**	**+0.07**
M3								
A96/99	**+0.46**	**−0.05**	**−0.05**	**+0.25**	**+0.17**	**+0.08**	**+0.36**	**+0.21**
Extrapolated RM05	−0.03	+0.01	0.0	−0.01	−0.02	0.0	**−0.05**	+0.01
C10+RM05	+0.01	0.0	0.0	−0.01	+0.01	−0.01	+0.01	0.0
Kurucz only	+0.01	**−0.08**	**+0.06**	**−0.09**	**+0.11**	**−0.10**	**−0.05**	**−0.15**
M15								
A96/99	**+0.44**	+0.02	**−0.17**	–	**+0.15**	**+0.12**	**+0.34**	**+0.25**
Extrapolated RM05	**−0.07**	0.0	+0.02	–	−0.03	+0.04	**−0.06**	−0.03
C10+RM05	0.0	0.0	+0.01	–	+0.01	0.0	0.0	−0.01
Kurucz only	**+0.14**	0.0	**−0.05**	+0.02	**+0.05**	+0.04	**+0.10**	**−0.06**

Notes: Extrapolated relations carry the CTRs outside the colour ranges in which they were calibrated. Abundance differences are calculated relative to the baseline abundances in Table 3, as described in Section 3.3.
References: A96 – Alonso et al. (1996); A99 – Alonso et al. (1999); RM05 – Ramirez & Melendez (2005); C10 – Casagrande et al. (2010).

(vi) the [Ti I/Fe I] ratio is moderately affected by temperature, while [Ti II/Fe II] is affected primarily by microturbulence (though the [Ti/Fe] errors are all <0.1 dex); the surface gravity effects are negligible;

(vii) the [Ba II/Fe II] and [Eu II/Fe II] ratios are most affected by temperature and microturbulence, though [Ba II/Fe II] is constrained to within 0.12 dex, while [Eu II/Fe II] is within 0.07 dex.

Thus, the systematic errors from the intrinsic uncertainties in atmospheric parameters are $\lesssim$0.1 dex for [Fe I/H], [Fe II/H], [Ti I/Fe I], [Ti II/Fe II], [Ba II/Fe II], and [Eu II/Fe II], and are <0.05 dex for [Ca I/Fe I] and [Ni I/Fe I].

Of course, the atmospheric parameters are not independent. It is thus instructive to see how the final abundances change as two parameters are varied together – these tests were performed only on 47 Tuc (which has the largest individual offsets). For each element ratio, the two parameters that individually showed the strongest changes in Table A1 were varied *together*. The maximum differences for all abundance ratios are shown at the bottom of Table A1.

These results show that within the 1σ boxes, [Ni I/Fe I] is negligibly affected by the atmospheric parameters, while [Ca I/Fe I] and [Ti I/Fe I] are moderately affected ($\lesssim$0.1 dex). The [Fe I/H], [Fe II/H], [Ti II/Fe II], [Ba II/Fe II], and [Eu II/Fe II] ratios are all significantly ($0.1 < \Delta[X/Fe] < 0.22$) affected by the changes in atmospheric parameters.

A2 Colour–temperature relations

In a CMD-based analysis, the observed stellar colours are transformed to effective temperatures via colour–temperature relations (CTRs). Several studies have calibrated these relations for different photometric filters and different stellar types, over ranges in colour and metallicity. This appendix investigates the effects on the abundances caused by changing these CTRs. To investigate metallicity dependencies, 47 Tuc, M3, and M15 were used for these tests. The relations of Alonso et al. (1996, 1999, for dwarfs and giants, respectively), Ramirez & Melendez (2005, for dwarfs and giants), and Casagrande et al. (2010, for dwarfs only – the Ramírez & Melendez relation was used for giants) are considered. Recall that for the abundances presented in MB08, Paper I, and Section 3 the ($B - V$) relations of Alonso et al. (1996, 1999) were used for 47 Tuc, while the ($V - I$) relations from Ramirez & Melendez (2005) were used for the other clusters. The CTRs are only valid for the regions in which they were calibrated; for stars whose colours fall outside the calibrated regions, MB08 and Paper I utilized the Kurucz grid of stellar models to determine effective temperatures. The effects of extrapolated relations and only values from the Kurucz grid are also considered.

Table A2 shows the offsets that occur when different CTRs are used. With the exception of the Kurucz only case, the differences for 47 Tuc are all negligible ($\lesssim$0.03 dex). The M3 and M15 results are *very* discrepant when the Alonso et al. (1996, 1999) relations are employed. This is consistent with the large offsets between the Alonso et al. (1996, 1999) CTRs versus the Ramirez & Melendez (2005) and Casagrande et al. (2010) CTRs. Of the three relations, the Ramirez & Melendez (2005) and Casagrande et al. (2010) relations are likely to be more accurate, since Alonso et al. had to rely on uncertain transformations between photometric systems (see the discussion by Casagrande et al. 2010). The Kurucz only relations are also quite discrepant, suggesting that empirical relations (specifically the Ramirez & Melendez 2005 and/or Casagrande et al. 2010 CTRs) may be a better choice for CMD-based studies.

Other than the large offsets from the ($V - I$) Alonso et al. (1996, 1999) relations and from the Kurucz only abundances, the differences from the other relations (including the extrapolated relations) are insignificant, except for [Ba II/Fe II], which is affected by ∼0.05 when the Ramirez & Melendez (2005) relation is extrapolated outside the calibrated regions in M3 and M15.

A3 Different photometric data sets

This appendix investigates the effects of different photometric data sets (i.e. V, I instead of B, V, taken with different instruments at different times). This test is only performed on 47 Tuc because B, V CMDs of the cores are not available for the other GCs. Recall that the original 47 Tuc abundances were found with the B, V photometry from Guhathakurta et al. (1992). Fig. A1(a) presents the boxes for the *HST* 47 Tuc V, I CMD from the ACS Galactic Globular Cluster Treasury (e.g. Sarajedini et al. 2007). The CTRs of Ramirez &

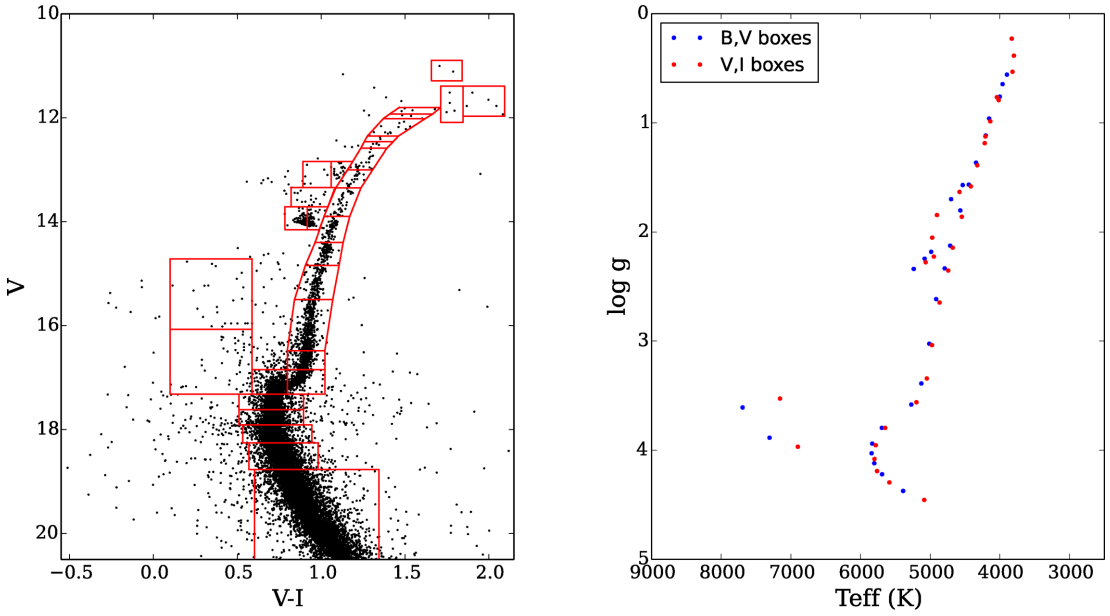

(a) V, I CMD

(b) HRD for B, V and V, I photometry

Figure A1. The V, I photometry for 47 Tuc. Left: the 30 CMD boxes and the Johnson V, I photometry from the ACS Galactic Globular Cluster Treasury (Sarajedini et al. 2007). Right: an HRD of the B, V (blue) and V, I (red) CMD boxes.

Table A3. Differences in CMD-based abundance ratios as a result of various alterations to the input photometry.

	Δ[Fe I/H]	Δ[Fe II/H]	Δ[Ca I/Fe I]	Δ[Ti I/Fe I]	Δ[Ti II/Fe II]	Δ[Ni I/Fe I]	Δ[Ba II/Fe II]	Δ[Eu II/Fe II]
V, *I* data								
47 Tuc	−0.04	**+0.07**	−0.02	−0.04	−0.04	+0.01	**−0.07**	+0.02
Completeness								
47 Tuc	**+0.07**	**+0.07**	+0.01	**+0.06**	**+0.07**	+0.04	**+0.07**	+0.03
M3	0.0	+0.01	+0.01	0.0	0.0	+0.01	−0.01	0.0
M13	−0.01	0.0	−0.01	−0.01	+0.01	−0.01	0.0	+0.01
NGC 7006	+0.03	+0.01	**−0.05**	+0.01	+0.02	−0.02	+0.01	0.0
M15	−0.03	0.0	−0.02	+0.03	+0.01	+0.04	0.0	−0.01
Sampling								
M15	**<0.22**	**<0.10**	**<0.09**	**<0.06**	**<0.10**	<0.03	**<0.21**	**<0.09**

Notes: Abundance differences are calculated relative to the baseline abundances in Table 3, as described in Section 3.3.

Melendez (2005) were used to determine atmospheric parameters for the V, I photometry; an HRD showing the box averages for the two data sets is shown in Fig. A1(b). The agreement between the parameters of each box is generally good, with the exception of the brightest RGB and blue straggler boxes.

The bright RGB boxes in the V, I CMD contain M giants. Because of TiO blanketing and the breakdown of the M giant $(B - V)$ CTR the M giants appear mixed with the K giants in the B, V CMD. For this reason, M giants need to be treated differently if a B, V CMD is employed. MB08 showed that, for the core of 47 Tuc, the TiO blanketing in the M giant spectra significantly reduced their impact on the IL spectrum, such that only small errors in the derived abundances would result from the omission of the two M giants.[12] The M giants were *not* removed from the V, I photometry, which accounts for the differences in the brightest boxes.

The differences in blue stragglers are likely only due to sampling. These boxes represent a small ($\lesssim$1 per cent) portion of the total light, and therefore have an insignificant effect on the final abundances. Small variations between B, V and V, I photometry may also be due to the Bond–Neff effect (Bond & Neff 1969), since 47 Tuc does have a significant population of CN-strong stars.

The abundance differences are listed in Table A3. In general, these differences are not drastic, with the exception of [Fe I/H] and [Ba II/Fe II], which differ by ∼0.07 dex. The small differences in Fe I and Ba II and the negligible differences in the other abundances indicate that the M giants do not need to be removed from the V, I data, and that (as in MB08) the TiO molecular lines do not need to be included for GCs at 47 Tuc's metallicity. Only 47 Tuc was considered for this test – however, variations between B, V and V, I may be metallicity dependent, or dependent upon the populations in a given GC.

[12] However, the mostly negligible abundance effects of the two M giants in the 47 Tuc spectrum may not translate to similar effects in more metal-rich GCs, which have a larger fraction of M giants. Therefore the presence of M giants needs to be considered carefully when analysing the IL spectra of GCs more metal rich than 47 Tuc.

A4 Incompleteness

Even the highest quality *HST* data suffer from incompleteness of the faintest stars. The effects of incompleteness were tested by increasing the numbers of stars in the lower main sequence boxes in order to match the theoretical luminosity functions (assuming no mass segregation; this means that this test may add too many low-mass stars). The abundance differences (tabulated in Table A3) are all $\lesssim$0.1 dex. The only GC affected by incompleteness is 47 Tuc; it is also the GC whose IL spectrum covers the smallest portion of the cluster (see Table 1), suggesting that mass segregation may be more important for 47 Tuc than for the other clusters. In 47 Tuc, the [Fe I/H], [Fe II/H], [Ti I/Fe I], [Ti II/Fe II], and [Ba II/Fe II] ratios are affected by <0.1 dex – the other abundances are largely unaffected.

A5 Sampling the input photometry

This appendix investigates the effects if the input photometry does not perfectly match the population observed in the IL spectra. This is especially problematic in cases where the spectrograph fibres must be scanned across the cluster. The input photometry can be cleaned based on distance from the cluster centre, but irregular coverage patterns (see Paper I) will lead to differences between the input photometry and the observed population.

As a test of this effect, it is assumed that there are no constraints on the area that was scanned in M15's wedge-shaped coverage pattern. Note that this is a somewhat unrealistic worst-case scenario; however, it serves as a useful test of how sensitive the abundances are to stochastic effects on the upper RGB. To select the input photometry, one hundred 80° wedges were selected by assuming a random[13] starting angle between 0° and 360°. ILABUNDS was then rerun on each of the 100 wedges, producing new abundances for each run. The largest offsets from the mean are listed in Table A3. The abundance differences can be quite large, especially for [Fe I/H] and [Ba II/Fe II], where the maximum offsets are ∼0.2 dex. However, the [Fe II/H], [Ca I/Fe I], [Ti II/Fe II], [Ni I/Fe I], and [Eu II/Fe II] abundances are less sensitive to this effect (with maximum differences $\lesssim$0.1 dex). The primary differences between each run are the numbers and properties of bright RGB stars. Thus, these tests indicate that [Fe I/H] and [Ba II/Fe II] are particularly sensitive to sampling of the upper RGB.

This test on M15's wedge-shaped pointing pattern illustrates the importance of adequately selecting stars that truly match the observed population. The relative numbers of stars at various evolutionary stages are important, as are slight differences in colours and magnitudes. Because each cluster is unique, this effect cannot be removed through a differential analysis. However, observations that cover more of the cluster (e.g. extragalactic observations) or whose pointing patterns are more regular (e.g. in the case of M3, M13, and NGC 7006) will not suffer from the problem as severely as M15, since the sampling differences between photometric data sets will be less extreme. Note, however, that the IL observations of M3, M13, NGC 7006, and M15 utilized discrete pointings across the cluster (see Paper I), albeit with short integration times. This means that the IL spectra are non-trivially weighted by the stars at those pointings. This effect is extremely difficult to account for – however, as the exposure times were short and the uncovered areas were small, this effect should not be too large.

In a CMD-based analysis of resolved GCs sampling problems can be alleviated by (1) symmetrically observing GCs and (2) using deep photometry that has been accurately sampled to match the IL spectra. Unfortunately, the second option is not possible for unresolved extragalactic targets. The next appendix investigates systematic offsets that occur when populations are unresolved, and have to be modelled with theoretical isochrones.

APPENDIX B: SYSTEMATIC OFFSETS THAT OCCUR IN AN HRD-BASED ANALYSIS

CMDs cannot be obtained for unresolved clusters, and theoretical isochrones must be used to generate HRDs (i.e. temperatures and surface gravities) for the underlying populations. The main advantage of an HRD-based analysis is that the stars are modelled in the theoretical plane, and there is no need to convert observable properties to physical quantities. The main disadvantage in a HRD-based analysis of an unresolved target is that very little is known about the GC a priori, and diagnostics must be used to revise the model of the underlying stellar population. This appendix investigates systematic errors that occur when the stellar populations are incorrectly modelled. These errors include

(i) uncertainties in identifying the best-fitting isochrones (Appendix B1);
(ii) uncertainties that occur when the theoretical isochrones are populated with stars (Appendix B2);
(iii) uncertainties in modelling evolved stars (Appendices B3 and B4) and main-sequence stars (Appendices B5 and B6).

Discrepancies between the real population and the modelled population may vary between clusters in the same study, making it difficult to remove these effects though differential analyses. Finally, the case of a partially resolved GC is investigated in Appendix B7.

B1 HRD-based abundances

MB08 and Colucci et al. (2009, 2011, 2012, 2013) have pioneered high-resolution IL spectral analyses of unresolved GCs. Their algorithm for identifying the HRD that best represents an underlying stellar population involves iterating upon isochrone parameters until the following criteria are met:

(i) the isochrone [Fe/H] matches the output integrated [Fe I/H] ratio;
(ii) any trends in Fe I abundance with wavelength, reduced EW (REW),[14] or excitation potential (EP) are minimized (similar to individual stellar analyses; see MB08);
(iii) the line-to-line abundance spreads from Fe I and Fe II lines are minimized.

Colucci et al. have demonstrated that a best-fitting HRD can be identified based on these criteria. Furthermore, Cameron (2009) argue that HRD-based abundances of Galactic GCs are in good agreement with CMD-based ones (which are, in turn, in agreement with literature abundances from individual stars). This paper focuses on the abundance uncertainties that arise as a result of uncertainties in identifying the best input isochrones.

First, the best-fitting standard BaSTI isochrones are identified for the targets GCs. No modifications were made to the default BaSTI HBs (see Appendix B3). As in Colucci et al, isochrones

[13] A random value was selected using NUMPY's RANDOM routines.

[14] REW = EW/λ.

Table B1. Parameters of the 'best-fitting' HRDs, and abundance comparisons with the CMD-based abundances.

	Age	[*Z*/H]	Δ[Fe I/H]	Δ[Fe II/H]	Δ[Ca I/Fe I]	Δ[Ti I/Fe I]	Δ[Ti II/Fe II]	Δ[Ni I/Fe I]	Δ[Ba II/Fe II]	Δ[Eu II/Fe II]
47 Tuc	10	−0.35	**+0.07**	**+0.19**	**−0.05**	**−0.10**	−0.01	+0.02	**−0.05**	**−0.08**
M3	9	−1.27	**−0.05**	−0.04	−0.01	**−0.20**	**−0.05**	−0.03	**−0.10**	**−0.06**
M13	12	−1.27	**−0.11**	**−0.13**	+0.03	**−0.19**	**−0.10**	−0.04	**−0.12**	−0.02
NGC 7006	7	−1.27	**+0.06**	−0.02	−0.02	**−0.14**	**+0.05**	−0.03	+0.03	**−0.05**
M15	9	−1.79	+0.02	**+0.06**	−0.01	−0.04	0.0	+0.01	+0.04	+0.03

Notes: Abundance differences are calculated relative to the CMD-based abundances in Table 3, as described in Section 3.3.

Table B2. Abundance ranges when all acceptable HRD solutions are considered.

	Δ[Fe I/H]	Δ[Fe II/H]	Δ[Ca I/Fe I]	Δ[Ti I/Fe I]	Δ[Ti II/Fe II]	Δ[Ni I/Fe I]	Δ[Ba II/Fe II]	Δ[Eu II/Fe II]
47 Tuc	**<0.12**	**<0.12**	**<0.07**	**<0.13**	**<0.12**	<0.03	**<0.19**	**<0.08**
M3	**<0.08**	**<0.15**	<0.04	**<0.07**	**<0.05**	<0.04	**<0.10**	**<0.05**
M13	**<0.06**	<0.02	<0.01	**<0.06**	**<0.05**	<0.01	**<0.06**	<0.02
NGC 7006	**<0.07**	**<0.16**	**<0.07**	**<0.12**	**<0.08**	<0.04	**<0.08**	<0.03
M15	**<0.16**	**<0.05**	**<0.05**	<0.02	**<0.05**	<0.03	**<0.10**	**<0.07**

Notes: Abundance differences are calculated relative to the best-fitting HRD abundances in Table B1.

with extended AGBs and mass-loss parameters of $\eta = 0.2$ were initially adopted (see Appendix B4 for tests with other AGB prescriptions, though note that MB08 utilize $\eta = 0.4$ isochrones based on the tests by Maraston 2005). In order to match 47 Tuc's observed luminosity function MB08 manually enhanced the number of AGB stars; no AGB enhancements were included in these tests. When the [Ca I/Fe I] ratio indicated α-enhancement, α-enhanced isochrones were used. The 'best-fitting' solution was deemed to be the one for which all slopes are minimized – note that this choice is subjective, since the slopes are rarely simultaneously minimized.

Table B1 presents the parameters for the best-fitting HRDs and comparisons with the CMD-based abundances. Note that none of the REW slopes are sufficiently flat for M15. With the exception of M13, all solutions are younger than isochrone fits indicate (see e.g. Dotter et al. 2010; VandenBerg et al. 2013). The best-fitting HRD abundances can be significantly offset from the CMD-based abundances – in particular, the [Ti I/Fe I] values are persistently lower than those from the CMD analyses and those from individual stars. The [Fe I/H], [Fe II/H], [Ti II/Fe II], [Ba II/Fe II], and [Eu II/Fe II] ratios are also significantly affected. Only [Ca I/Fe I] and [Ni I/Fe I] agree well with the CMD-based abundances.

B1.1 Uncertainties in identifying the best HRDs

The best-fitting HRDs are those which *best* meet the above criteria; however, multiple solutions meet these criteria, and there is a range of possible abundances. In this appendix, the selection criteria of Colucci et al. are broadened to assess the possible abundance ranges.

The first two criteria for identifying the best HRD each have associated uncertainties. Not only does the integrated [Fe I/H] have its own uncertainty, there may be systematic offsets between spectroscopically determined [Fe/H] values and between those determined from isochrone fits – these [Fe/H] values could be off by as much as 0.2 dex.[15] Additionally, [Fe I/H] is not necessarily indicative of the cluster [Fe/H], because of NLTE effects. Thus, it may not be ideal to force the integrated [Fe I/H] abundance to equal the isochrone [Fe/H].

The least-squares fits to the Fe I abundances versus wavelength, REW, and EP also have their own uncertainties, such that multiple solutions produce flat fits (i.e. with no significant trend in the Fe I abundances). Furthermore, the dispersion in Fe I abundances ensures that multiple solutions can produce sufficiently flat slopes, even in individual stellar analyses. This means that it may not be reasonable to consider only the isochrones that produce the flattest slopes.

Possible HRD solutions are identified in a similar way as Colucci et al.

(i) BaSTI isochrones of all ages and metallicities were used to generate synthetic stellar populations.

(ii) For each cluster, ILABUNDS was run on the synthesized population.

(iii) Any isochrones whose output [Fe I/H] ratios were within 0.2 dex of the input isochrone [Fe/H] were deemed to be possible solutions. Note that Colucci et al. find the best [Fe/H] solution for each age; for the purposes of this errors analysis, *all* possible [Fe/H]/age combinations are retained if they meet this criterion.

(iv) For each possible solution, the fits to the Fe I abundance versus wavelength, REW, and EP were calculated. All solutions whose slopes were $|m| \leq 0.04$ (within the uncertainty) were considered to be alternate solutions.

Table B2 presents the maximum offsets of the alternate solutions from the best-fitting HRD solutions. The spreads around the best-fitting HRD abundances are quite large, with every element except Ni having significant differences. The [Ca I/Fe I] and [Eu II/Fe II] ratios are still fairly robust, with differences of 0.07 and 0.08 dex, respectively. The other abundances ratios can be significantly affected by the isochrone parameters, depending on the cluster. It is also important to note that the offsets from the CMD-based abundances are sometimes larger than the uncertainties quoted in Table B2, suggesting that there is some systematic offset between the two methods.

[15] For example, from high-resolution spectroscopic analyses of M3, Cohen & Melendez (2005) find an average [Fe/H] ~ -1.4 while Sneden et al. (2004) find [Fe/H] ~ -1.6. Isochrone fits with the DSED isochrones also indicate values of [Fe/H] ~ -1.6 (Dotter et al. 2010).

Table B3. Abundance offsets with different isochrones.

	Δ[Fe I/H]	Δ[Fe II/H]	Δ[Ca I/Fe I]	Δ[Ti I/Fe I]	Δ[Ti II/Fe II]	Δ[Ni I/Fe I]	Δ[Ba II/Fe II]	Δ[Eu II/Fe II]
47 Tuc								
Victoria–Regina	+0.02	+0.03	−0.01	+0.01	0.0	0.0	0.0	0.0
DSED [α/Fe] =0.2	+0.02	−0.01	+0.01	+0.02	+0.01	0.0	+0.03	+0.01
DSED [α/Fe] =0.4	+0.03	+0.02	−0.01	+0.02	0.0	+0.01	+0.02	+0.02
M3								
Victoria–Regina	−0.01	+0.04	−0.01	−0.01	−0.01	+0.01	−0.01	−0.01
DSED [α/Fe] =0.2	**−0.15**	**−0.06**	+0.02	**−0.09**	**−0.05**	−0.04	**−0.11**	**−0.07**
DSED [α/Fe] =0.4	**−0.05**	+0.04	−0.02	−0.01	−0.04	+0.03	**−0.06**	−0.03
M15								
Victoria–Regina	−0.01	+0.04	0.0	−0.04	0.0	−0.02	0.0	−0.02
DSED [α/Fe] =0.2	**−0.35**	**−0.14**	**+0.13**	**+0.07**	**−0.14**	−0.01	**−0.27**	**−0.14**
DSED [α/Fe] =0.4	**+0.05**	+0.04	−0.02	−0.03	+0.01	0.0	**+0.05**	+0.04

Notes: Abundance differences are calculated relative to the abundances derived with the BaSTI isochrones and resolved boxes of the HB and AGB (see the text).

Table B4. Abundance differences as a result of the input IMF.

	Δ[Fe I/H]	Δ[Fe II/H]	Δ[Ca I/Fe I]	Δ[Ti I/Fe I]	Δ[Ti II/Fe II]	Δ[Ni I/Fe I]	Δ[Ba II/Fe II]	Δ[Eu II/Fe II]
47 Tuc								
Salpeter	−0.04	0.0	−0.01	−0.04	−0.04	0.0	**−0.05**	−0.03
Chabrier	−0.04	−0.01	−0.02	**−0.06**	**−0.05**	−0.02	**−0.07**	**−0.05**
M3								
Salpeter	+0.02	0.0	0.0	+0.04	+0.01	+0.01	+0.02	+0.02
Chabrier	+0.01	−0.01	0.0	+0.03	+0.01	+0.01	+0.02	+0.02
M15								
Salpeter	+0.03	0.0	−0.01	**−0.08**	+0.01	+0.01	+0.02	+0.02
Chabrier	+0.01	0.0	0.0	**−0.06**	0.0	+0.02	0.0	+0.02

Notes: Abundance differences are calculated relative to the best-fitting HRD abundances in Table B1.

B1.2 Comparisons between different isochrones

Different sets of isochrones predict slightly disparate distributions of stars in an HRD, even for a common age and metallicity, which could lead to slight discrepancies in the integrated abundances. Here the DSED and Victoria–Regina isochrones (see Section 2.4.2) are compared to the BaSTI isochrones. Tests are run on 47 Tuc, M3, and M15 to investigate metallicity effects. Because neither the DSED nor the Victoria–Regina models include evolved HB or AGB stars in their models, the HB/AGB boxes from the resolved photometry are used instead of HRD boxes, *in all cases* (even with the BaSTI isochrones). The isochrones were sampled such that the number of RGB stars agreed with the number of resolved RGB stars – this was necessary to ensure that the relative number of HB/AGB and RGB stars was approximately correct. The isochrones with the best-fitting BaSTI parameters (from Appendix B1) were used.

The offsets from the BaSTI abundances are shown in Table B3. The differences between the BaSTI and Victoria–Regina isochrones are insignificant in all cases. The DSED isochrones have larger offsets at low [Fe/H], depending on the input [α/Fe] ratio. The BaSTI and Victoria–Regina models use [α/Fe] =+0.4 and +0.3, respectively, while DSED isochrones can have [α/Fe] =+0.2 or +0.4. The [α/Fe] =+0.4 DSED isochrones are in much better agreement than the +0.2 ones, although the [α/Fe] =+0.4 isochrone offsets can be ∼0.05 dex. This suggests that the slight differences in the treatment of the upper RGB, subgiant branch, and main-sequence turn-off do not have a strong effect on any of the final, integrated abundances, though the input [α/Fe] abundance may be important.

B2 Populating an isochrone

An isochrone provides the temperature and surface gravity at certain mass intervals for a cluster of a given age and chemical composition. To determine the integrated abundances of a cluster, ILABUNDS must also know the number of stars in each mass bin. Stars are assigned to each mass bin assuming that the stellar masses are distributed according to an initial mass function (IMF; Appendix B2.1), with the total number of stars determined from a cluster's total absolute *V* magnitude (Appendix B2).

B2.1 IMF

For their analyses of unresolved systems, MB08 and Colucci et al. utilize a Kroupa (2002) IMF. However, other forms of the IMF exist, for example the Salpeter (1955) and Chabrier (2003) IMFs, which differ most from the Kroupa IMF at the high-mass end ($M \gtrsim 0.5\,M_{\odot}$). These alternate IMFs are used to assign stars to the best-fitting HRDs from Appendix B1. The abundance differences are shown in Table B4. The different IMFs have no significant effect on M3. For 47 Tuc, the Salpeter IMF only significantly alters the [Ba II/Fe II] abundance (by 0.05 dex), while the Chabrier IMF has a $0.05 \lesssim \Delta[X/Fe] < 0.1$ dex effect on [Ti I/Fe I], [Ti II/Fe II], [Ba II/Fe II], and [Eu II/Fe II]. The [Fe I/H] ratio is also slightly affected by the Chabrier IMF. M15's [Ti I/Fe I] ratios are affected by both IMFs. These results suggest that Fe I, Ti, Ba, and Eu are sensitive to the sampling of the highest mass stars.

Table B5. Abundance offsets when the GC total magnitude is adjusted.

	Δ[Fe I/H]	Δ[Fe II/H]	Δ[Ca I/Fe I]	Δ[Ti I/Fe I]	Δ[Ti II/Fe II]	Δ[Ni I/Fe I]	Δ[Ba II/Fe II]	Δ[Eu II/Fe II]
47 Tuc								
$\Delta M_{V,\,obs} = +1$	−0.03	+0.02	−0.03	**−0.06**	**−0.05**	−0.02	**−0.07**	**−0.05**
$\Delta M_{V,\,obs} = +0.5$	+0.04	0.0	+0.01	**+0.05**	+0.03	+0.01	+0.04	+0.03
$\Delta M_{V,\,obs} = -0.5$	+0.02	0.0	0.0	+0.01	+0.02	0.0	+0.02	+0.01
$\Delta M_{V,\,obs} = -1$	+0.01	0.0	−0.01	0.0	+0.01	0.0	0.0	0.0
M3								
$\Delta M_{V,\,obs} = +1$	**+0.36**	**+0.05**	0.0	**+0.41**	**+0.14**	**+0.10**	**+0.33**	**+0.23**
$\Delta M_{V,\,obs} = +0.5$	**+0.21**	+0.02	+0.02	**+0.29**	**+0.08**	**+0.06**	**+0.20**	**+0.14**
$\Delta M_{V,\,obs} = -0.5$	**+0.06**	0.0	+0.01	**+0.10**	+0.03	+0.02	**+0.06**	**+0.05**
$\Delta M_{V,\,obs} = -1$	**+0.06**	+0.02	0.0	**+0.05**	+0.02	+0.01	+0.04	+0.02
M15								
$\Delta M_{V,\,obs} = +1$	**+0.25**	**+0.10**	**−0.10**	**+0.05**	**+0.07**	**+0.07**	**+0.20**	**+0.15**
$\Delta M_{V,\,obs} = +0.5$	**+0.12**	+0.04	**−0.05**	+0.03	+0.03	+0.04	**+0.10**	**+0.07**
$\Delta M_{V,\,obs} = -0.5$	**−0.11**	0.0	+0.02	**−0.21**	−0.02	**−0.07**	**−0.10**	**−0.08**
$\Delta M_{V,\,obs} = -1$	−0.03	+0.02	0.0	**−0.14**	0.0	−0.04	−0.03	−0.03

Notes: Abundance differences are calculated relative to the best-fitting HRD abundances in Table B1. Note that most of the abundance offsets for the low-magnitude clusters are dramatically reduced if fractional stars are used to populate the HRDs.

B2.2 Total magnitude

The total magnitude of the observed portion of the GC, $M_{V,\,obs}$, determines the total number of stars in the populated HRD. Fainter GCs will have fewer stars to populate the HRD; certain boxes along the isochrone may then have no stars while others may be rounded up to one star, and the relative flux contributions from the boxes will be disrupted. This is shown in Table B5, where the abundance differences from the best-fitting HRD values are shown when different values of $M_{V,\,obs}$ are considered.

It is clear from Table B5 that lowering the total magnitude (i.e. making the cluster brighter) only leads to small offsets ($\lesssim$0.1 dex) while making the cluster fainter can lead to large offsets in the [Fe I/H], [Ti I/Fe I], [Ba II/Fe II], and [Eu II/Fe II] ratios ($0.1 < \Delta[X/Fe] < 0.4$ dex, with the largest differences occurring for M13 and M15). The [Fe II/H], [Ca I/Fe I], [Ti II/Fe II], and [Ni I/Fe I] ratios are somewhat affected ($\lesssim$0.1 dex) when the GC is made fainter. These abundance differences are driven by how the isochrone is populated, such that fainter GCs cannot adequately populate the upper RGB.

This test indicates that fainter clusters will be more susceptible to abundance offsets if the cluster M_V is not well constrained. These problems can be reduced by using photometry of the bright RGB, AGB, and HB stars, and/or by sampling as much of the GC as possible. However, additional tests show that these errors can be dramatically reduced if *fractional* stars are used to populate the HRDs, instead of integer numbers of stars. Although this choice is distinctly non-physical it seems to work for IL spectra of bright, well-sampled GCs. Whether it will be applicable to real, intrinsically poorly sampled GCs is uncertain.

B3 Horizontal branch morphology

As discussed in Paper I, it is difficult to model the HBs of unresolved GCs, given the uncertain effects of the 'second parameter' (Dotter 2008; Dotter et al. 2010). Synthetic HBs with a range of morphologies can be generated (e.g. from the BaSTI data base), but require inputs for the average HB mass and the spread in HB masses, both of which are not known a priori and may not exactly match the true HB stars. In particular, if blue HB stars are not properly accounted for, spectroscopic ages will be skewed to younger ages to compensate for the absence of the hot stars (e.g. Lee, Yoon & Lee 2000; Ocvirk 2010). At high resolution, MB08 argued that blue HB stars could also confuse trends in Fe I abundances with EP, leading to incorrect [Fe/H] and age determinations.

It is therefore possible that HB morphology could measurably affect the derived chemical abundances. Lower resolution studies have concluded that IL spectral features can help constrain HB morphology, e.g. the Balmer line ratios (Schiavon et al. 2004) or specific indices from ionized atoms (e.g. the Mg II doublet at 2800 Å or the Ca II H&K index; Percival & Salaris 2011). However, the IL spectra presented here do not extend blueward enough to access these features.

The purpose of the tests presented below is not to identify or test the best way to constrain HB morphology, but to isolate and examine the abundance effects from HB morphology. With an M31 GC at [Fe/H] = −2.2, Colucci et al. (2009) tested the effects of HB morphology by manually moving red HB stars to blue HB star boxes in their best-fitting HRDs. For that particular GC, they found that individual Fe I abundances changed by <0.05 dex and that the effect on the best-fitting isochrone parameters was negligible. Here these results are tested on the Galactic GCs.

B3.1 The direct effects of HB stars on abundances

To test the direct effects of HB morphology on chemical abundances, the IL spectra and resolved photometry of the second parameter triad M3, M13, and NGC 7006 are used. The HB boxes for the three GCs are swapped, while maintaining the same total number of HB stars for each cluster. Worst-case scenarios of purely red and purely blue HBs were also considered for M13 and NGC 7006, respectively. Finally, synthetic HBs from the BaSTI data base were assigned to M13 and NGC 7006, using masses of 0.5 and 0.8 $M_\odot$ and mass dispersions of 0.02 $M_\odot$. These differences are shown in Table B6; they are first organized by GC, then by HB morphology.

Table B6 shows that the following.

(i) The slight differences between M3 and NGC 7006's HBs lead to negligible abundance offsets.

(ii) HBs that are too red raise the integrated [Fe I/H], while HBs that are too blue lower the [Fe I/H]. The largest differences are ∼0.1 dex.

Table B6. Abundance differences as a result of HB morphology.

	Δ[Fe I/H]	Δ[Fe II/H]	Δ[Ca I/Fe I]	Δ[Ti I/Fe I]	Δ[Ti II/Fe II]	Δ[Ni I/Fe I]	Δ[Ba II/Fe II]	Δ[Eu II/Fe II]
M3								
M13's HB	**−0.05**	0.0	0.0	0.0	−0.02	−0.01	**−0.06**	−0.02
NGC 7006's HB	0.0	0.0	0.0	+0.01	−0.01	+0.01	−0.01	+0.01
M13								
Purely blue HB	−0.04	−0.02	0.0	+0.01	−0.03	+0.01	−0.04	+0.01
Synthetic blue	**−0.06**	**−0.09**	+0.02	−0.01	+0.01	−0.04	−0.03	−0.02
M3's HB	**+0.06**	−0.01	−0.01	+0.01	+0.02	0.0	**+0.05**	**+0.05**
NGC 7006's HB	**+0.07**	−0.01	−0.01	+0.01	0.0	0.0	**+0.05**	**+0.06**
Synthetic red	+0.02	**−0.17**	−0.01	**+0.05**	**−0.06**	+0.02	+0.01	**+0.11**
Purely red HB	+0.02	**−0.08**	−0.02	**+0.08**	**−0.07**	+0.04	−0.01	**+0.10**
NGC 7006								
Purely blue HB	**−0.11**	−0.02	−0.01	+0.03	**−0.07**	+0.02	**−0.11**	**−0.04**
Synthetic blue	**−0.08**	−0.02	0.0	+0.02	−0.03	+0.01	**−0.07**	−0.03
M13's HB	**−0.07**	0.0	0.0	+0.01	−0.03	0.0	**−0.07**	**−0.05**
M3's HB	0.0	0.0	0.0	+0.01	0.0	0.0	−0.01	−0.02
Synthetic red	−0.03	**−0.05**	0.0	+0.04	−0.03	+0.03	−0.03	+0.01
Purely red HB	−0.04	−0.04	−0.01	**+0.06**	**−0.05**	+0.03	**−0.05**	+0.01

Notes: Abundance differences are calculated relative to the baseline abundances in Table 3, as described in Section 3.3. Tests are organized by cluster, then by HB morphology, with the bluest HBs listed first.

Table B7. Abundance differences and parameters of the best-fitting HRDs when synthetic HBs are used.

	Age	[Z/H]	Δ[Fe I/H]	Δ[Fe II/H]	Δ[Ca I/Fe I]	Δ[Ti I/Fe I]	Δ[Ti II/Fe II]	Δ[Ni I/Fe I]	Δ[Ba II/Fe II]	Δ[Eu II/Fe II]
M3										
Red HB	8	−0.96	**+0.11**	**+0.05**	−0.02	**+0.15**	0.0	**+0.07**	**+0.11**	**+0.12**
Blue HB	14	−1.27	**+0.08**	+0.01	+0.02	**+0.16**	**+0.07**	+0.03	**+0.12**	**+0.06**
M13										
Red HB	12	−1.27	**+0.18**	−0.02	−0.02	**+0.20**	**+0.05**	**+0.05**	**+0.16**	**+0.13**
Blue HB	14	−1.27	**+0.10**	+0.04	0.0	**+0.10**	**+0.08**	0.0	**+0.10**	+0.02
NGC 7006										
Red HB	5	−0.96	**+0.13**	**+0.06**	0.0	**+0.10**	+0.03	**+0.05**	**+0.14**	**+0.09**
Blue HB	14	−0.96	+0.02	**+0.28**	−0.03	**−0.12**	+0.01	+0.01	−0.04	**+0.08**
M15										
Red HB	14	−1.79	**+0.06**	−0.02	−0.03	**+0.06**	+0.01	**+0.07**	+0.03	**+0.08**
Blue HB	14	−1.79	+0.01	+0.03	0.0	+0.02	+0.02	0.0	0.0	−0.01

Notes: Abundance differences are calculated relative to the best-fitting HRD-based abundances in Table B1.

(iii) The [Fe II/H] ratios are most affected when red HB stars are added (or when intermediate HB stars are removed). The largest offsets are ∼0.2 dex.

(iv) The [Ca I/Fe I] and [Ni I/Fe I] ratios are mostly unaffected by HB morphology.

(v) The [Ti/Fe] ratios are significantly affected only when the HBs are significantly different from reality (e.g. the pure and synthetic red cases for M13).

(vi) The total offsets in [Ba II/Fe II] are $\lesssim$0.1 dex. HBs that are too blue lower the output [Ba II/Fe II]. However, HBs that are too red do not always raise [Ba II/Fe II], because of the varying effects on Fe II. When intermediate HB stars are added to M13, the [Ba II/Fe II] ratio is increased; when they are removed or altered in M3 and NGC 7006 [Ba II/Fe II] is decreased. It therefore appears that [Ba II/Fe II] is most affected by the presence or absence of intermediate HB stars. This is not only driven by the [Fe II/H] abundance.

(vii) HBs that are too blue lower [Eu II/Fe II], while redder HBs raise [Eu II/Fe II]. Again, these effects are not driven by [Fe II/H] differences.

The alternate HBs also affect the trends of Fe I abundances with wavelength, REW, and EP, such that the slopes are generally made steeper when the HB is improperly modelled. These slope changes imply that different HB models will lead to alternate best-fitting isochrones.

B3.2 The indirect effects of HB stars on isochrone age and [Fe/H]

To test the indirect effects of HB stars on isochrone age and [Fe/H], the default HBs were replaced with extremely blue and extremely red synthetic HBs (from the BaSTI synthetic HB generator), and ILABUNDS was rerun on the new populations. The parameters of the new isochrones and the subsequent abundance offsets are shown in Table B7.

These results show that for the GCs with intermediate HB morphologies (M3 and NGC 7006), HBs that are too red lead to underpredictions of the GC age (most likely to compensate for the lack of hot, blue stars in the models) while HBs that are too blue lead to overpredictions of the GC age (likely for the opposite reason).

Table B8. Abundance differences from modelling the AGB.

AGB[a]	Isochrone Age[b]	[Fe/H]	Δ[Fe I/H]	Δ[Fe II/H]	Δ[Ca I/Fe I]	Δ[Ti I/Fe I]	Δ[Ti II/Fe II]	Δ[Ni I/Fe I]	Δ[Ba II/Fe II]	Δ[Eu II/Fe II]
47 Tuc										
E-0.4	10[c]	−0.70	+0.01	+0.02	−0.03	−0.04	−0.01	−0.01	−0.03	−0.03
N-0.2	10[c]	−0.70	+0.03	+0.02	−0.01	+0.01	+0.01	+0.01	+0.02	+0.01
N-0.4	10[c]	−0.70	**+0.07**	0.0	+0.01	**+0.06**	**+0.06**	+0.01	**+0.08**	**+0.05**
E-0.4	11	−0.70	+0.03	0.0	−0.01	+0.01	+0.01	+0.01	+0.02	+0.02
N-0.2	12	−0.70	+0.01	+0.03	−0.02	−0.01	−0.01	0.0	−0.03	−0.02
N-0.4	11	−0.60	+0.03	**+0.09**	**−0.05**	−0.04	−0.02	+0.01	−0.04	−0.03
M3										
E-0.4	9[c]	−1.62	**+0.06**	+0.03	0.0	0.0	+0.04	+0.02	**+0.05**	+0.01
N-0.2	9[c]	−1.62	**+0.14**	+0.01	+0.02	**+0.23**	**+0.06**	**+0.05**	**+0.15**	**+0.10**
N-0.4	9[c]	−1.62	**+0.18**	+0.02	+0.01	**+0.22**	**+0.09**	**+0.05**	**+0.19**	**+0.11**
E-0.4	10	−1.62	+0.04	+0.02	0.0	0.0	+0.03	+0.01	+0.03	0.0
N-0.2	8	−1.31	**+0.08**	**+0.15**	+0.04	**+0.08**	−0.01	**+0.06**	**+0.05**	**+0.07**
N-0.4	10	−1.31	**+0.10**	**+0.15**	−0.03	**+0.09**	0.0	**+0.07**	**+0.08**	**+0.08**
M15										
E-0.4	9[c]	−2.14	**−0.16**	0.0	+0.03	**−0.38**	−0.01	**−0.13**	**−0.14**	**−0.13**
N-0.2	9[c]	−2.14	+0.03	0.0	−0.01	+0.01	+0.02	+0.02	+0.02	+0.02
N-0.4	9[c]	−2.14	**+0.13**	+0.03	−0.03	**−0.06**	**+0.08**	−0.03	**+0.11**	+0.04
E-0.4	10	−2.62	**−0.19**	+0.01	+0.03	**−0.06**	−0.04	**−0.11**	**−0.18**	**−0.14**
N-0.2	8	−2.14	+0.01	0.0	0.0	+0.02	+0.01	+0.01	0.0	+0.01
N-0.4	10	−2.62	**+0.10**	+0.02	−0.03	**−0.09**	**+0.05**	0.0	+0.07	+0.04

Notes: Abundance differences are calculated relative to the best-fitting HRD abundances in Table B1, which were determined with extended, $\eta = 0.2$ isochrones. Tests are organized by cluster, then by AGB prescription, with the original isochrone age and [Fe/H] listed first, followed by the new, best-fitting HRD.

[a]The AGB prescription indicates which BaSTI isochrones were utilized. 'E-0.4' denotes extended, $\eta = 0.4$ isochrones, 'N-0.2' denotes normal, $\eta = 0.2$ isochrones, and 'N-0.4' denotes normal, $\eta = 0.4$ isochrones.

[b]Ages are in Gyr.

[c]These tests utilized the original, best-fitting isochrone parameters from Appendix B1.1.

These findings agree well with the findings of Lee et al. (2000) and Ocvirk (2010), i.e. that when blue HB stars are not properly accounted for, IL analyses will converge on ages that are too young. For M13 and M15 (the clusters with blue HBs) the extreme blue and extreme red cases both converge on old ages. To understand this effect, the default HB morphologies of the original best-fitting isochrones must be investigated. For M13 and M15 the original HBs are significantly redder than the real HBs; M15's default HB also extends slightly blueward of the synthetic red HB tested here. The fact that the synthetic pure red and blue HBs both push the isochrones to old ages suggests that the presence (or absence) of intermediate HB stars have a more significant effect than the bluest HB stars. This agrees with the findings of Colucci et al. (2009), who tested these effects on a GC with both blue and red HB stars and found that the bluest HB stars had a negligible effect. Thus, convergence on a correct age (within ∼5 Gyr) requires modelling the intermediate age HB stars (at least approximately) correctly.

However, regardless of how the HBs are modelled, all isochrones converge on reasonable isochrone metallicities. Furthermore, certain abundance ratios are relatively insensitive to the adopted isochrone age. While [Fe I/H], [Ti I/Fe I], [Ba II/Fe II], and [Eu II/Fe II] are very sensitive to changes in HB morphology (with offsets $\gtrsim$0.1 dex), [Ca I/Fe I], [Ti II/Fe II], and [Ni I/Fe I] are much less sensitive, with offsets <0.1 dex.

B4 Asymptotic giant branch stars

With the BaSTI isochrones the AGB can be modelled in various ways. First, different mass-loss parameters of $\eta = 0.2$ or 0.4 can be selected. Second, the AGB can be extended through all thermal pulse phases or can be terminated after the first few pulses (where the former is denoted as the 'extended' case and the latter as the 'normal' case; see the BaSTI website). Given their tests with Galactic GCs (Cameron 2009), Colucci et al. utilize extended AGB isochrones with $\eta = 0.2$. This appendix investigates the abundance offsets that arise when the other AGB prescriptions are used. Note that MB08 required an enhancement in the number of AGB stars in order to match the observed luminosity function and abundances of 47 Tuc. That enhancement is not included here.

B4.1 The direct effects of AGB stars on abundances

The AGB prescriptions were first altered while maintaining the best-fitting isochrone parameters from Appendix B1.1. These offsets are shown in Table B8. The AGB prescription has a small effect on 47 Tuc's abundances, and a much larger effect on M3 and M15's abundances. The ratios that are most affected by the AGB models are [Fe I/H], [Ti I/Fe I], [Ba II/Fe II], and [Eu II/Fe II] (with offsets ∼0.1–0.2 dex, depending on the cluster), while [Fe II/H], [Ti II/Fe II], and [Ni I/Fe I] are occasionally affected (0.1–0.15 dex). For all GCs, the [Ca I/Fe I] ratio is largely insensitive ($\lesssim$0.05 dex) to the AGB prescription.

The abundance offsets are not the same for a given AGB prescription. For 47 Tuc, only the normal, $\eta = 0.4$ case significantly alters the abundances. For M3 both of the normal AGB cases ($\eta = 0.2$ and 0.4) lead to large offsets, while for M15 both $\eta = 0.4$ cases create significant offsets. In some cases the various AGB prescriptions bring the HRD-based abundances into better agreement with

Table B9. The effects of blue stragglers.

	Δ[Fe I/H]	Δ[Fe II/H]	Δ[Ca I/Fe I]	Δ[Ti I/Fe I]	Δ[Ti II/Fe II]	Δ[Ni I/Fe I]	Δ[Ba II/Fe II]	Δ[Eu II/Fe II]
47 Tuc	+0.02	0.0	0.0	0.0	+0.02	−0.01	+0.01	+0.01
M3	+0.02	**+0.07**	0.0	0.0	−0.03	+0.01	−0.03	**−0.06**
M13	+0.03	+0.04	−0.02	−0.02	−0.02	−0.02	−0.03	−0.03
NGC 7006	+0.02	+0.01	+0.01	−0.01	+0.02	−0.01	+0.02	0.0
M15	**+0.07**	+0.02	−0.02	−0.04	−0.04	−0.03	**+0.05**	+0.01

Notes: Abundance differences are calculated relative to the best-fitting HRD abundances in Table B1.

Table B10. The effects of a lower mass cut-off.

	Age	[Z/H]	Δ[Fe I/H]	Δ[Fe II/H]	Δ[Ca I/Fe I]	Δ[Ti I/Fe I]	Δ[Ti II/Fe II]	Δ[Ni I/Fe I]	Δ[Ba II/Fe II]	Δ[Eu II/Fe II]
47 Tuc	10	−0.35	**−0.05**	0.0	−0.04	**−0.07**	**−0.07**	−0.03	**−0.09**	**−0.12**
M3	9	−1.27	**+0.10**	−0.03	+0.02	**+0.24**	+0.03	+0.04	**+0.11**	**+0.10**
M13	11	−1.27	**+0.10**	−0.02	−0.01	**+0.16**	+0.02	+0.01	**+0.07**	**+0.08**
NGC 7006	5	−0.96	**+0.09**	**+0.12**	0.0	**+0.10**	0.0	**+0.05**	**+0.08**	**+0.09**
M15	9	−1.79	**−0.13**	**−0.05**	+0.04	−0.01	−0.04	−0.01	**−0.11**	**−0.05**

Notes: Abundance differences are calculated relative to the best-fitting HRD abundances in Table B1.

the CMD-based abundances; for example, normal AGBs raise M3's [Ti I/Fe I] ratio; however, other abundance ratios are then sometimes brought out of agreement. Thus, the systematic uncertainties from a given AGB prescription are not the same for all clusters, and adopting a uniform treatment of the AGB will not remove intracluster systematic offsets. Without resolved photometry of the brightest AGB stars, it would be difficult to determine which AGB prescription is most representative of a given cluster.

B4.2 The indirect effects of AGB stars on isochrone age and [Fe/H]

To test how the AGB models affect the parameters for the best-fitting HRDs, the isochrone parameters were allowed to vary. These new best-fitting parameters for each AGB prescription and the resulting abundance differences are also shown in Table B8. In all cases new ages and/or metallicities are favoured, though they are not significantly different from the original values. This indicates that the AGB prescription is not responsible for the young isochrone ages for M3 and M15.

When the new isochrone parameters are selected for a given AGB treatment, the abundances are generally brought into *slightly* better agreement with the original HRD-based abundances, particularly for 47 Tuc. For example, the large offsets in [Fe I/H], [Ti I/Fe I], [Ba II/Fe II], and [Eu II/Fe II] from assuming the original age and [Fe/H] are generally (though not always) reduced when new best-fitting HRDs are adopted. However, in some cases the offsets are still quite large (e.g. with M3's 'normal' AGBs), illustrating that the treatment of the AGB could be problematic for high-resolution optical IL spectral studies of unresolved GCs.

B5 Blue stragglers

Isochrones do not contain models for blue stragglers (the stars that appear to lie on the main sequence, blueward of the turn-off). Though there are few of these stars, they are brighter and hotter than main-sequence stars, and thus may have a non-negligible effect on the IL spectral lines. To test these effects the resolved blue straggler boxes were included with the best-fitting isochrones. The results are shown in Table B9, and are generally quite small, except for a few cases where [Fe I/H], [Fe II/H], [Ba II/Fe II], and [Eu II/Fe II] are affected by up to 0.07 dex. This suggests that the inclusion of blue stragglers is not essential for the majority of elements, though the singly ionized elements are mildly sensitive to them. Furthermore, the blue stragglers have only a slight effect on the Fe I trends with wavelength, REW, and EP, and therefore do not have a significant effect on the isochrone age.

B6 Lower mass cut-off

In their IL analysis of 47 Tuc, MB08 found that a lower mass cut-off was necessary to reproduce the observed luminosity function (ostensibly because the IL spectrum only covers the cluster core, and mass segregation must be taken into account). This appendix investigates the effects of applying a lower mass cut-off such that all stars fainter than $M_V = +4.7$ are removed from the synthetic HRD – this was the cut-off adopted by MB08 to match 47 Tuc's observed luminosity function. (Note that this test is essentially the opposite of the incompleteness test in Appendix A4, except that now new isochrones are identified.) This cut-off was applied to all the GCs, even though some of the IL spectra cover out to further radii where there may still be fainter stars. New best-fitting isochrones were then identified.

The new isochrone parameters and the abundance offsets from the original best-fitting HRDs are shown in Table B10. With the lower mass cut-off, the same isochrones are identified for 47 Tuc, M3, and M15; for M13 a slightly younger isochrone is preferred, while for NGC 7006 a more metal-rich, younger isochrone is preferred. Note that the slopes are never sufficiently flat for M15, as with the original best-fitting HRD (Appendix B1.1). The [Fe I/H], [Ti I/Fe I], [Ba II/Fe II], and [Eu II/Fe II] ratios are particularly affected (up to ∼0.1–0.2 dex) by the absence of the lowest mass stars. However, this may be because more high-mass stars are needed to maintain the same total cluster magnitude.

B7 Partially resolved clusters

So far, the tests on HRD abundances have shown that the uncertainties in HB, AGB, RGB, and lower main-sequence stars can be prohibitively large, with uncertainties as high as 0.4 dex in [Fe I/H]

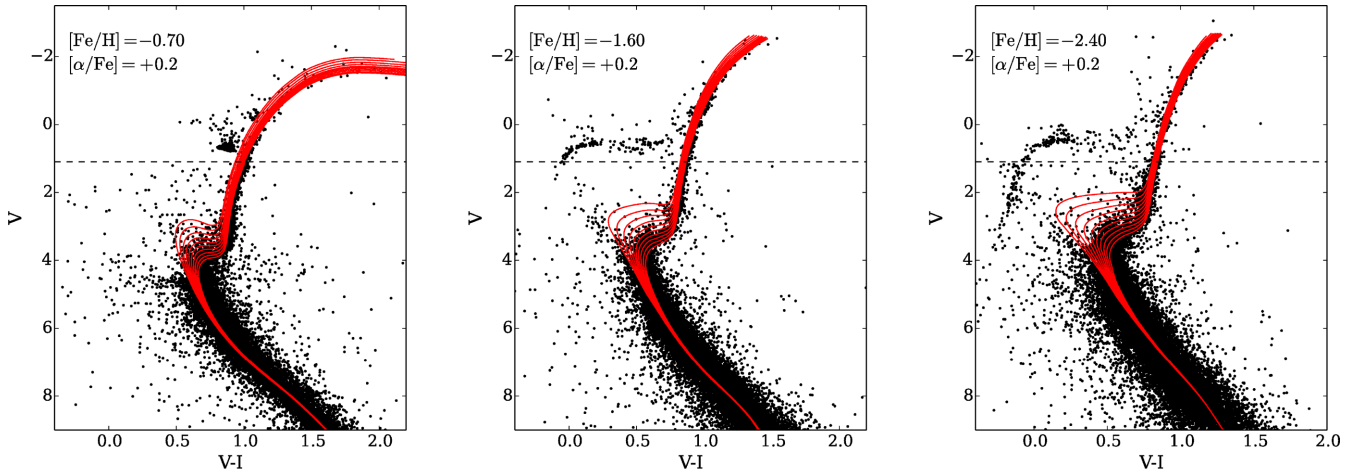

(a) 47 Tuc (b) M3 (c) M15

Figure B1. Examples of isochrones that might be used in an analysis of a partially resolved cluster. Here it is assumed that the GCs can only be observed to just below the HB, i.e. to the dashed line. The isochrones are from the DSED (Dotter et al. 2008) and have ages of 5, 6, 7, 8, 9, 10, 11, 12, 13, and 14 Gyr.

Table B11. Abundance differences with a partially resolved cluster.

Age (Gyr)	[*Z*/H]	Δ[Fe I/H]	Δ[Fe II/H]	Δ[Ca I/Fe I]	Δ[Ti I/Fe I]	Δ[Ti II/Fe II]	Δ[Ni I/Fe I]	Δ[Ba II/Fe II]	Δ[Eu II/Fe II]
47 Tuc									
11	−0.35	**+0.09**	**+0.17**	**−0.06**	**−0.12**	0.0	+0.03	−0.04	**−0.08**
M3									
13	−1.27	−0.04	**−0.15**	+0.04	−0.03	+0.02	**−0.06**	−0.03	−0.01
M13									
13	−1.27	**−0.05**	**−0.12**	**+0.06**	−0.04	−0.03	**−0.05**	**−0.07**	−0.04
NGC 7006									
10	−1.27	+0.04	**+0.08**	+0.03	**−0.11**	**+0.09**	**−0.08**	+0.04	**−0.07**
M15									
10	−1.79	0.0	**+0.06**	+0.01	−0.03	+0.01	−0.03	+0.02	−0.01

Notes: All isochrones have [α/Fe] = +0.2. Abundance differences are calculated relative to the CMD-based abundances in Table 3, as described in Section 3.3.

and [Ti I/Fe I], 0.3 dex in [Ba II/Fe II], 0.2 dex in [Fe II/H], and 0.1 dex in [Ca I/Fe I], [Ti II/Fe II], and [Ni I/Fe I] (depending on the cluster). Observations of clusters outside of the MW and its dwarf satellite systems can provide photometry of the brightest stars in a cluster; the HB morphology, AGB prescription, etc. can then be characterized, eliminating or reducing many of these uncertainties. However, even with partial photometry, stars fainter than the HB still contribute a significant amount of light to the IL spectra (see tables 4 – 8 in Paper I). Furthermore, stars in cluster *cores* may not be resolvable. Given the large errors associated with sampling uncertainties, it may be preferable to model the stellar populations with stellar isochrones that can be refined based on the resolved photometry. This appendix investigates the effects of combining observations of the upper CMD with models of the lower HRD.

The [Fe/H] of a partially resolved cluster can be estimated through comparisons with Galactic GC fiducials (e.g. Mackey et al. 2013). The [Fe/H] of the input isochrone can then be refined based on the output from ILABUNDS, as for completely unresolved clusters. Furthermore, a partially resolved GC's age can be somewhat constrained from the upper CMD. Here the 'best-fitting' HRDs are found for all target GCs, adopting the criterion that the isochrone must fit the 'observed portion' of the CMD (taken to be the portion down to the bottom of the HB).

Initially, the best-fitting [Fe/H] values from the BaSTI isochrones (see Appendix B1) were chosen, since they fit the upper RGBs well (see Fig. B1). Synthetic HBs were selected to best match the observed HB. The isochrones were populated and the default HBs were replaced with the synthetic ones. ILABUNDS was then rerun on the new stellar populations.

The differences from the CMD-based abundances are shown in Table B11. All GCs converge on isochrone ages that agree slightly better with results from resolved photometry. For M3, M13, NGC 7006, and M15 (whose HB's were not modelled accurately with the default isochrones), the addition of synthesized HBs has brought many of the abundances into better agreement with the CMD-based ones. For 47 Tuc, however, the synthetic HBs introduce larger discrepancies with the CMD-based values, suggesting that for red HB GCs the default BaSTI HBs are likely to be sufficient. NGC 7006's [Ti I/Fe I] ratio remains discrepant, suggesting that the population is still not perfectly modelled.

Note that for nearby extragalactic clusters the *faint* detection limit will be just below the HB, and the photometric uncertainties will be much larger than in Fig. B1. This means it will not be as easy to constrain the best-fitting metallicities from the CMDs. However, even if incorrect isochrone metallicities are chosen for these GCs,

the abundances converge back on reasonable metallicities for the Galactic GCs.

APPENDIX C: SYSTEMATIC OFFSETS THAT OCCUR IN ALL IL ANALYSES

Regardless of how the stellar population is modelled, some simplifying assumptions must be made. These include

(i) the methods used to generate the stellar parameters (Appendices C1 and C2);
(ii) the models of stellar subpopulations (Appendices C3 and C4);
(iii) the influence of foreground stars (Appendix C5) and chemical variations in the model atmospheres (Appendix C6).

Again, the validity of these assumptions can differ between GCs in a given study. This appendix tests specific assumptions that will affect both CMD- and HRD-based analyses.

C1 CMD/HRD boxes

In both CMD- and HRD-based methods the stars are binned together to reduce computation time. The effects from the coarseness and definition of the boxes are investigated here. First, an abundance analysis is performed on 47 Tuc with *no* CMD boxes (i.e. EWs are computed for each star). The abundance differences (tabulated in Table C1) are completely negligible, suggesting that boxing the CMD is an appropriate choice to speed up computations. This is essential, since using the default number of 27 boxes speeds up computations by a factor of 200 compared to the no box case.

Box definition was then investigated with 47 Tuc and M13, to compare the effects of metallicity and HB morphology. Finer and coarser boxes are shown in Fig. C1 with the old 47 Tuc and M13 boxes (in black). The finer boxes were reshaped to provide finer coverage of the upper RGB, HB, and AGB, and to include more stars in the main-sequence boxes. The coarser boxes still maintain finer resolution of the brightest stars. These abundance differences are also shown in Table C1. As expected, the differences are negligible for the cases with finer boxes. For the coarser boxes, the differences are significant for 47 Tuc when 5–17 boxes are considered while M13 is sensitive to the coarse five box case. A moderate number of boxes (∼25–40) therefore provides a compromise between faster computing time and precision. In fact, using the default number of boxes (∼30) only slows computations down by a factor of 2 over the coarsest box cases.

These tests were then performed on the synthetic HRDs. The original HRD-based abundances in Table B1 were produced using isochrones that were binned into boxes that each contained 3.5 per cent of the total luminosity. Table C1 also shows the effects if these HRD boxes are redefined. For 47 Tuc, boxes of 2–20 per cent lead to insignificant differences. Surprisingly, the 1 per cent boxes have large offsets – this seems to be a result of rounding errors when individual boxes are assigned fractions of stars instead of round numbers (as discussed in Appendix B2.2). M13 is much more sensitive to HRD box definitions, though the 2 per cent case seems to still be due to rounding errors. Thus, these results indicate that the HRD-based abundances are also largely insensitive (with offsets $\lesssim$0.05 dex) to the precise box definitions.

C2 The microturbulence relation

Each box's microturbulent velocity is determined through an empirical relation with the surface gravity; this relationship is based on a fit to Arcturus and the Sun (see MB08 for details). ILABUNDS was rerun with alternate empirical microturbulence relations from Kirby et al. (2009, K09, calibrated to GC and dwarf galaxy stars)

Table C1. Differences in 47 Tuc abundance ratios as a result of different boxing methods.

	Δ[Fe I/H]	Δ[Fe II/H]	Δ[Ca I/Fe I]	Δ[Ti I/Fe I]	Δ[Ti II/Fe II]	Δ[Ni I/Fe I]	Δ[Ba II/Fe II]	Δ[Eu II/Fe II]
47 Tuc: CMD								
No boxes	0.0	+0.0	+0.01	+0.01	+0.01	+0.01	+0.01	+0.02
Finer boxes (49)	−0.01	0.0	+0.01	+0.01	0.0	+0.01	0.0	+0.04
Coarse boxes (17)	−0.01	+0.01	+0.01	+0.01	0.0	0.0	0.0	**+0.05**
Coarser boxes (5)	−0.02	0.0	+0.02	+0.03	−0.01	+0.01	0.0	**+0.07**
M3: CMD								
Finer boxes (40)	−0.03	+0.01	0.0	0.0	−0.01	0.0	−0.03	0.0
Coarse boxes (16)	−0.01	+0.02	+0.01	+0.01	0.0	0.0	−0.01	+0.01
Coarser boxes (5)	**+0.09**	**+0.08**	+0.02	+0.04	+0.04	0.0	**+0.05**	+0.03
47 Tuc: HRD								
1 per cent	**−0.07**	+0.04	**−0.06**	**−0.14**	**−0.10**	−0.04	**−0.17**	**−0.12**
2 per cent	−0.01	+0.01	−0.02	−0.03	−0.01	−0.01	−0.04	−0.03
5 per cent	+0.01	−0.01	0.0	+0.02	+0.01	0.0	+0.01	+0.02
10 per cent	−0.01	0.0	0.0	0.0	−0.01	0.0	+0.02	0.0
20 per cent	−0.01	−0.02	+0.01	+0.03	0.0	+0.01	+0.01	+0.03
M13: HRD								
1 per cent	**+0.11**	+0.01	−0.01	**+0.16**	+0.03	+0.03	**+0.09**	**+0.06**
2 per cent	**+0.05**	0.0	0.0	**−0.06**	−0.03	−0.01	**−0.05**	−0.04
5 per cent	**−0.09**	−0.02	+0.02	−0.04	−0.04	−0.01	**−0.07**	**−0.05**
10 per cent	−0.03	−0.03	0.0	0.0	−0.03	0.0	−0.03	0.0
20 per cent	+0.04	0.0	−0.01	+0.04	−0.01	+0.02	+0.02	+0.02

Notes: CMD-based abundance differences are calculated relative to the baseline abundances in Table 3, as described in Section 3.3, and use 27 boxes for 47 Tuc and 33 boxes for M13. HRD-based abundance differences are calculated relative to the best-fitting HRD-based values in Table B1, and use box sizes of 3.5 per cent.

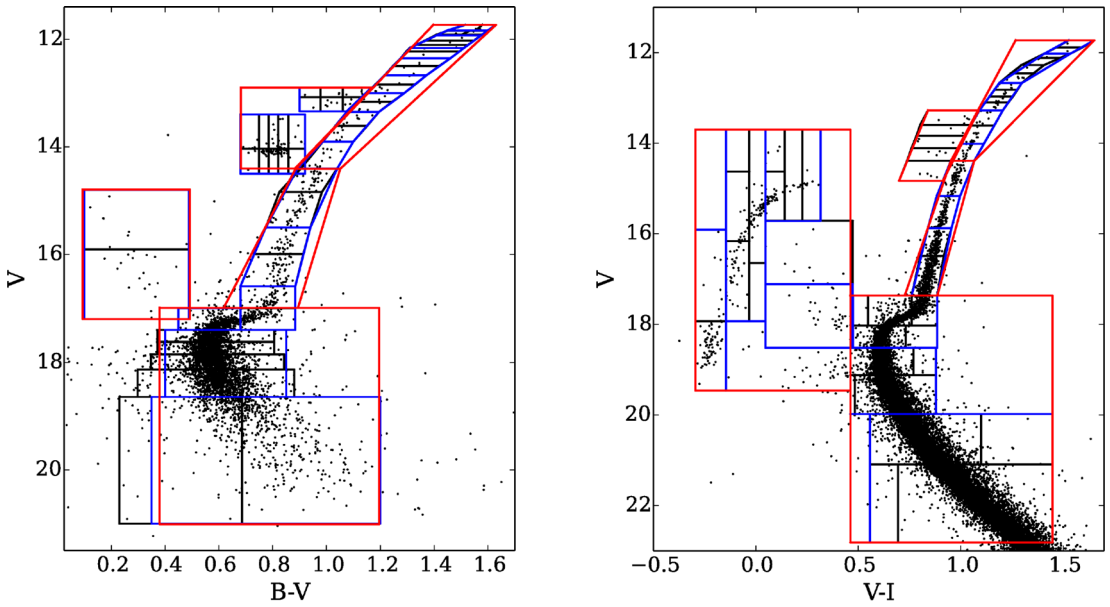

(a) 47 Tuc boxes (b) M13 boxes

Figure C1. Comparisons of box definitions for 47 Tuc (left) and M13 (right). Finer boxes (in black) have increased resolution on the RGB, HB, and AGB. Coarser boxes are shown in blue and red.

and Gratton, Carretta & Castelli (1996, G96). Note that the MB08 and K09 relations are only dependent on log g, though the G96 relation is dependent on log g and $T_{\rm eff}$. The differences in these relations will lead to slight variations in the subpopulations.

The abundance offsets are shown in Table C2 for 47 Tuc, M3, and M15 (to investigate [Fe/H] effects). With the exception of Ba II, the largest abundance differences are all $\lesssim$0.1 dex. The differences between abundances with the MB08 and K09 relations are mostly insignificant, supporting that the small offset is negligible. The G96 relation has a significant effect on all abundances, depending on the cluster, where the offsets are largest for M15. It is not clear if it is valid to extend this relationship to the hottest stars in the blue HB clusters.

The 'real' microturbulent velocities are dispersed about these relations. Furthermore, each box contains stars with a dispersion of microturbulent velocities. To test these effects, each star in a given box was assigned the same microturbulence value, which was randomly selected from a Gaussian distribution with a standard deviation of 0.2 dex, centred on the MB08 relation. These microturbulence values were reselected 100 times. The maximal abundance offsets (also shown in Table C2) are $\lesssim$0.1 dex, with [Ba II/Fe II] having the greatest difference.

C3 Anomalous stars

Some cluster stars are distinctly different from the other cluster stars. This appendix investigates the effects of two different types of oddball stars: long period variables (Appendix C3.1) and carbon-enhanced stars (Appendix C3.2).

C3.1 Long period variables

As discussed in MB08 and Appendix A3, the core region of 47 Tuc contains two bright, cool M giants. These stars are long period variables (LPVs), stars which exhibit large brightness variations over fairly long periods (days to years). These LPVs are only likely to exist in clusters at 47 Tuc's metallicity and above. MB08 showed that these M giants are troublesome in the B, V photometry because line blanketing reduces the B and V magnitudes such that the stars appear to lie further down the RGB; including those stars in boxes with incorrect atmospheric parameters led to large abundance offsets. This problem does not occur in the V, I photometry (see Appendix 2.4.1) – however, since the M giants are LPVs, their atmospheric parameters change over time, such that the properties of the M giants in the photometry/isochrone may not match the conditions that were present when the IL spectra was obtained.

The original V, I abundances were calculated with the two bright M giants at the tip of the RGB. To test the worst-case effects of long period variability, these two stars were moved to boxes that were 1 mag fainter. The abundance offsets (with respect to the abundances from the V, I photometry in Appendix 2.4.1) are shown in Table C3. The [Fe I/H], [Ti I/Fe I], [Ti II/Fe II], and [Ba II/Fe II] ratios are all significantly affected, though the differences are <0.1 dex. The other ratios are largely unaffected by the changes in the LPVs.

C3.2 Carbon-enhanced CH stars

Certain clusters (e.g. M15; Shetrone et al. 1999) have been observed to have anomalous bright stars with strong CH bands (which have been referred to as CH stars). To test the effects of these stars, the brightest star in M15 was made a CH star. Note that this is not the real CH star in M15; instead, this provides an indication of a worst-case scenario. During the EW analysis, the brightest star was assigned the [C/Fe], [N/Fe], and [O/Fe] abundances from Shetrone et al. (1999) and the standard cluster abundances for the lines of interest. These C, N, and O abundances are then included in the calculations for the continuous fluxes. Note that the effects of molecular lines would have to be investigated via spectrum syntheses (see Paper I).

The abundance offsets are shown in Table C3, and are insignificant for all elements.

Table C2. Differences in abundance ratios as a result of different microturbulence relations.

	Δ[Fe I/H]	Δ[Fe II/H]	Δ[Ca I/Fe I]	Δ[Ti I/Fe I]	Δ[Ti II/Fe II]	Δ[Ni I/Fe I]	Δ[Ba II/Fe II]	Δ[Eu II/Fe II]
47 Tuc								
MB08 with dispersion	**<0.08**	**<0.05**	<0.02	<0.02	**<0.06**	<0.01	**<0.09**	<0.03
Kirby et al. (2009)	**−0.07**	−0.04	−0.01	+0.01	**−0.05**	0.0	0.0	+0.04
Gratton et al. (1996)	**−0.13**	**−0.08**	−0.02	−0.03	**−0.10**	+0.01	**0.16**	**+0.06**
M3								
Kirby et al. (2009)	−0.04	−0.01	−0.01	+0.01	−0.04	0.0	−0.01	0.0
Gratton et al. (1996)	**−0.12**	**−0.05**	−0.03	+0.04	**−0.11**	0.0	**0.27**	+0.01
M15								
Kirby et al. (2009)	**−0.05**	0.0	+0.01	+0.04	−0.03	+0.03	−0.02	−0.03
Gratton et al. (1996)	**−0.21**	−0.01	**+0.05**	**+0.18**	**−0.10**	**+0.11**	**−0.30**	**+0.06**

Notes. Abundance differences are calculated relative to the baseline abundances in Table 3, as described in Section 3.3.

Table C3. Differences in abundance ratios as a result of various assumptions about the underlying stellar population.

	Δ[Fe I/H]	Δ[Fe II/H]	Δ[Ca I/Fe I]	Δ[Ti I/Fe I]	Δ[Ti II/Fe II]	Δ[Ni I/Fe I]	Δ[Ba II/Fe II]	Δ[Eu II/Fe II]
LPVs[a]								
47 Tuc	+0.01	**+0.07**	0.0	+0.03	+0.01	+0.03	0.0	0.0
CH stars[a]								
M15	0.0	0.0	+0.01	0.0	0.0	+0.01	0.0	+0.01
Hot stars								
M13: abundances	**+0.06**	+0.04	−0.01	0.0	−0.01	−0.03	+0.04	−0.04
M13: rotation[a]	+0.02	+0.02	+0.01	−0.01	**+0.07**	+0.01	0.0	−0.02
Field stars[a]								
47 Tuc	**<0.09**	**<0.08**	**<0.09**	<0.04	**<0.07**	**<0.06**	**<0.10**	**<0.05**
NGC 7006	<0.04	<0.01	<0.0	<0.03	<0.02	<0.01	<0.03	<0.04
M15	**<0.10**	**<0.09**	<0.04	–[b]	<0.02	<0.03	**<0.07**	<0.04
ODFNEW atms								
47 Tuc	**−0.05**	**−0.12**	+0.03	+0.02	+0.02	−0.01	−0.01	+0.02
M3	0.0	**−0.07**	+0.01	+0.01	+0.02	−0.02	−0.02	−0.01
M13	0.0	**−0.07**	+0.01	+0.01	+0.03	−0.02	−0.02	−0.01
NGC 7006	0.0	**−0.07**	0.0	+0.02	+0.02	−0.01	−0.03	−0.03
M15	+0.02	−0.02	0.0	+0.01	+0.01	+0.01	0.0	−0.03
CN-cycled atms								
47 Tuc	**−0.05**	**−0.07**	0.0	−0.01	0.0	−0.01	−0.02	+0.01

Notes: Abundance differences are calculated relative to the baseline abundances in Table 3, unless otherwise noted.
[a]Baseline abundances were calculated separately (see text).
[b]Lines are too weak to measure in the synthesized spectra.

C4 Hot stars

The hottest stars in a cluster ($T_{\rm eff} \gtrsim 8000$ K) can have different properties from the other stars in the cluster. The effects of radiative levitation can drastically increase the surface abundances of hot stars, possibly increasing the metal-poor surface abundances of some elements to solar composition (e.g. Behr, Cohen & McCarthy 2000; Behr 2003; Lovisi et al. 2012). The hottest stars can also have high rotation (up to ∼60 km s^{-1}; Behr 2003), which broadens the line profiles and could affect the shape of an IL spectral line. In old GCs, the hottest stars are often blue HB stars, which do not contribute much to the IL – Paper I showed that these changes had a minimal effect on the synthesized Mg I, Na I, and Eu II lines. This appendix investigates the effects on the EWs of the Fe, Ca, Ti, Na, and Ba lines. Only M13 is considered for these tests, since 47 Tuc, M3, and NGC 7006 do not have hot stars.

C4.1 Surface composition

For this test, all stars hotter than 8000 K were given solar composition, while all stars cooler than 8000 K were assigned the standard cluster chemistry. EWs were calculated for each box and were combined as in the standard method – however, the initial abundances were preserved, and *no* iterations were done to match the observed EWs. ILABUNDS was then rerun on the new EWs. The differences from the original abundances provide indications of the effects of the hottest HB stars. These differences are listed in Table C3. With the exception of [Fe I/H], all abundance ratios are stable to within 0.04 dex.

C4.2 Rotation

For stellar rotation, the same approach was employed as in Appendix C4.1, except that stars hotter than 8000 K were assigned rotational

velocities of 60 km s^{-1} *and* solar abundances.[16] Since rotation affects the shape of the line profiles, lines were synthesized (in 10 Å regions around the line of interest). Again, the boxes were combined and a new synthetic IL spectra was produced. To automate this process, EWs of the lines in the new IL spectra were measured in DAOSPEC, and the new EWs were fed to ILABUNDS. Because the success of spectrum syntheses is highly dependent on the input line list, the same procedure was applied *without the rotation enhancement in the hot stars* – these abundances were used as the original abundances in the calculation of the abundance differences, which are shown in Table C3. Table C3 shows that, with the exception of [Ti II/Fe II], all abundances are stable to within 0.02 dex.

C5 Field stars

There is always the possibility that an interloping field star could contaminate the IL spectra from the cluster. For Galactic clusters these field stars would be in the MW – for extragalactic GCs these interloping field stars could also be in the host galaxy. To test the possible effects of field stars, the worst-case scenario is considered, i.e. that one of the brightest cluster stars is actually a field star. Three factors are varied.

(i) *Colour.* The field star is taken to be either the brightest star on the RGB, or the brightest blue star (which may not be included in any of the CMD boxes).
(ii) *Composition.* The field star is considered to be either solar metallicity or a metal-poor star (with [Fe/H] = −2.5). In the latter case the field star is assumed to be α-enhanced.
(iii) *Luminosity class.* The field star is taken to be either a dwarf or a giant. Physical parameters are then assigned to the field star based on isochrone fits with the DSED isochrones.

To test metallicity effects, 47 Tuc, NGC 7006, and M15 were all considered for these tests. Besancon models of the Galaxy[17] (Robin et al. 2003) were used to find the average radial velocity of a star at the same Galactic latitude and longitude as the target GC – the artificial field stars were then assigned these radial velocities. For each spectral line, synthetic spectra were generated for each CMD box (with the field star in its own box), EWs were remeasured in the combined synthetic spectrum, and ILABUNDS was rerun on the new EWs (this procedure is similar to that in Appendix C4.2). Because the input line lists are uncalibrated, the same procedure was performed on the original CMD boxes; those abundances serve as the baseline values for the comparisons.

The offsets are listed in Table C3, and are generally $\lesssim$0.1 dex. For these resolved GCs, the abundance differences are likely to be upper limits, since the worst-case scenarios were considered. For unresolved GCs a brighter field star of a vastly different colour could be included. Targets should therefore be inspected carefully for stellar contamination. Extragalactic GCs will have smaller Galactic field star contamination, but may also suffer from contamination from its host galaxy.

C6 Model atmosphere chemistry

C6.1 α-enhancement

Spectroscopic analyses typically adopt α-enhanced model atmospheres for metal-poor stars, since the [α/Fe] ratios in MW stars and clusters are enhanced (e.g. see Venn et al. 2004; Pritzl et al. 2005). To reflect this α-enhancement, the AODFNEW model atmospheres from the Kurucz data base have all α-elements (Ne, Mg, Si, S, Ar, Ca, and Ti) enhanced by 0.4 dex over the scaled-solar abundances.[18] These α-enhanced model atmospheres have therefore been used for the baseline abundances of the target Galactic GCs, which are known to be α-enhanced. The α-enhanced atmospheres have also been used for extragalactic targets whose α-abundances indicate enhancement (e.g. Colucci et al. 2009).

However, the IL abundance analyses have shown that some α-elements are *not* enhanced in IL, such as Mg (e.g. Colucci et al. 2009; Paper I). This has been interpreted as a chemical signature of the multiple populations in GCs, where there is a second population that is enriched in products from e.g. AGB nucleosynthesis. Thus, the abundances of e.g. O and Mg are expected to be lower in the second generation stars, as has been observed (e.g. Carretta et al. 2009). This has the effect of lowering the IL abundances if there are bright second generation stars. Since some of those elements are included in the model atmosphere α-enhancement, it may not be proper to use AODFNEW atmospheres for all stars. This effect is tested by using solar-scaled ODFNEW atmospheres instead of AODFNEW ones. The abundance differences are tabulated in Table C3. For the vast majority of elements the differences are insignificant. Only for Fe II does the α-enhancement make a difference, with offsets up to ∼0.1 dex. This is likely because for the brightest RGB stars, Fe II is the dominant ionization stage, and will be more affected by the presence or absence of free electrons.

C6.2 Heavily CN-cycled atmospheres

Stellar abundances (in particular, the C and N abundances) change as a star evolves up the RGB and proceeds through the HB and AGB phases. To test the worse case effects of C and N variations on the atmospheric opacities, the heavily CN-cycled MARCS atmospheres (Gustafsson et al. 2008) were adopted for all boxes with $\log g < 3.5$ dex (i.e. for all boxes that contained giants). The results are shown in Table C3, and are only significant for [Fe I/H] and [Fe II/H], though both are $\lesssim$0.07 dex.

SUPPORTING INFORMATION

Additional Supporting Information may be found in the online version of this article:

Table 2. The line list (http://mnras.oxfordjournals.org/lookup/suppl/doi:10.1093/mnras/stu1296/-/DC1).

Please note: Oxford University Press is not responsible for the content or functionality of any supporting materials supplied by the authors. Any queries (other than missing material) should be directed to the corresponding author for the article.

[16] Note that only considering rotation without enhanced abundances leads to no differences in spectral features.
[17] http://model.obs-besancon.fr/

[18] Note that the high solar O abundance means that O is actually enhanced by +0.54.

This paper has been typeset from a TEX/LATEX file prepared by the author.